学位論文

The Development and Application of a New 3-D Orbital Fitting Tool for Exoplanet Studies

(系外惑星の研究のための新しい三次元軌道決定ツールの開発と応用)

平成 28 年 7 月博士　(理学)　申請

東京大学大学院理学系研究科

天文学専攻

ミード カイル エーロン

Mede Kyle Aaron

"Imagination will often carry us to worlds that never were. But without it we go nowhere."

Carl Sagan

論文の内容の要旨

The Development and Application of a New 3-D Orbital Fitting Tool for Exoplanet Studies

(系外惑星の研究のための新しい三次元軌道決定ツールの開発と応用)

ミード カイル エーロン

I present ExoSOFT, a toolbox to fit the orbits of binary stars and exoplanets, along with its application to the V450 Andromedae and HR 8799 systems. With its ability to simultaneously fit radial velocity and astrometric data, ExoSOFT was used to find the complete Keplerian orbital solution of the companion to V450 Andromedae. The dynamical mass of the companion can only be obtained using both radial velocity and astrometric data. I find the companion to be a 0.28 $M_{\odot}$ star, and clearly not sub-stellar as previously reported. I also use ExoSOFT to investigate the coplanarity of the multi-planet system around HR 8799. My Markov Chain Monte Carlo analysis suggests that all four planets reside in a single orbital plane inclined by $\sim 35^{\circ}$, contrary to recent reports that planet d might show a strong mutual inclination of up to 20° with respect to the other three. Similarly, the orbital solutions are consistent with all four residing in circular orbits, with only planet c having a possible eccentricity $e > 0.08$ at the 1σ level. While there has yet to be a planetary mass companion for which both radial velocity and astrometric data are available, upcoming space and ground-based facilities will dramatically increase the number of potential candidates. The joint orbit fitting power and open source design of ExoSOFT will make it an increasingly useful tool to investigate the masses and orbital elements of newly discovered exoplanets.

Acknowledgements

I would like to first thank my beautiful wife and wonderful family for always supporting me in my endeavors. To Tim Brandt for being an incredible source of support and inspiration throughout all my graduate research projects. To my supervisor Motohide Tamura, for accepting me as a member of SEEDS and supporting me in many ways during my graduate studies. Lastly, I wish to express my appreciation to the faculty and staff at The University of Tokyo and all those who helped me get to this point.

K.M. gratefully acknowledges support from the Mitsubishi Corporation International Student Scholarship.

This research made use of the SIMBAD literature database, operated at CDS, Strasbourge, France, and of NASA's Astrophysics Data System. This research made use of the NASA/IPAC/NExScI Star and Exoplanet Database, which is operated by the Jet Propulsion Laboratory, California Institute of Technology, under contract with the National Aeronautics and Space Administration. This research has made use of the Exoplanet Orbit Database and the Exoplanet Data Explorer at exoplanets.org. This research has made use of the NASA Exoplanet Archive, which is operated by the California Institute of Technology, under contract with the National Aeronautics and Space Administration under the Exoplanet Exploration Program. This work is based in part on data collected at Subaru Telescope, which is operated by the National Astronomical Observatory of Japan. The data reductions presented here in part were performed with PyRAF and PyFITS, which are products of the Space Telescope Science Institute (STScI/AURA/NASA). The analysis presented here is also based on observations made with the NASA/ESA Hubble Space Telescope, and obtained from the Hubble Legacy Archive, which is a collaboration between the Space Telescope Science Institute, the Space Telescope European Coordinating Facility (ST-ECF/ESA) and the Canadian Astronomy Data Centre (CADC/NRC/CSA). Some of the data analysis were in part carried out on a common use data analysis computer system at the Astronomy Data Center, ADC, of the National Astronomical Observatory of Japan. This research has made use of the VizieR catalogue access tool and the SIMBAD database, which are operated at CDS, Strasbourg, France.

Finally, myself and all associated co-authors recognize and acknowledge the very significant cultural role and reverence that the summit of Maunakea has always had within the indigenous Hawaiian community. We are most fortunate to have the opportunity to conduct observations from this mountain.

Contents

This is dedicated to my family

Chapter 1

Introduction

The field of extrasolar planet (exoplanet) research has boomed over the past couple decades following the first confirmed discovery in 1992 [195]. Over this time, thousands of exoplanets have been found using both indirect and direct detection methods. As of June 2016, the complete collection of confirmed exoplanets totals nearly 3300[1], with orbital separations ranging from a few thousandths to a few thousand AU and planetary masses as small as that of Saturn's moon Titan (~ 0.02 $M_\oplus$). A subset of exoplanets with mass $\lesssim$13 M_J and separations $\lesssim$100 AU are plotted in Figure 1.1, including those found indirectly with transit photometry, Doppler radial velocity and gravitational microlensing (shown as red, blue and green dots respectively) and directly detected through high contrast imaging (shown in yellow). Their sensitivity to different areas of parameter space makes these techniques highly complementary; all have contributed to broadening our understanding of planetary systems in our galaxy.

Figure 1.1 demonstrates that indirect detection techniques are responsible for the majority of known exoplanets. Indirect detection relies on observations of the host stars themselves (for which photons can be collected quickly), and discerning the effect planets have on the stars' brightnesses or spectra. In addition, both transit photometry and gravitational microlensing surveys can observe a large number of stars simultaneously, further increasing detection frequencies. Interestingly, the unique nature of gravitational microlensing has led to the discovery of the most distant known exoplanets, with the furthest to date orbiting OGLE-2005-BLG-390L located almost 7000 pc from Earth [16]. On the other hand, the transit and radial velocity methods are most sensitive to short period companions whose orbits we view edge-on. In fact, 98%[2] of those found during the largest transit survey to date, *Kepler*, were $<10^\circ$ from edge-on. Planets at high inclinations simply do not transit. In the case of gravitational microlensing, as the review by Gaudi [72] admits, the events are rare, impossible to predict and typically last less than a day, making follow-up observations impossible. However, microlensing is likely the only way to find Earth-mass planets at separations wider than a few AU.

[1] exoplanetarchive.ipac.caltech.edu
[2] exoplanetarchive.ipac.caltech.edu

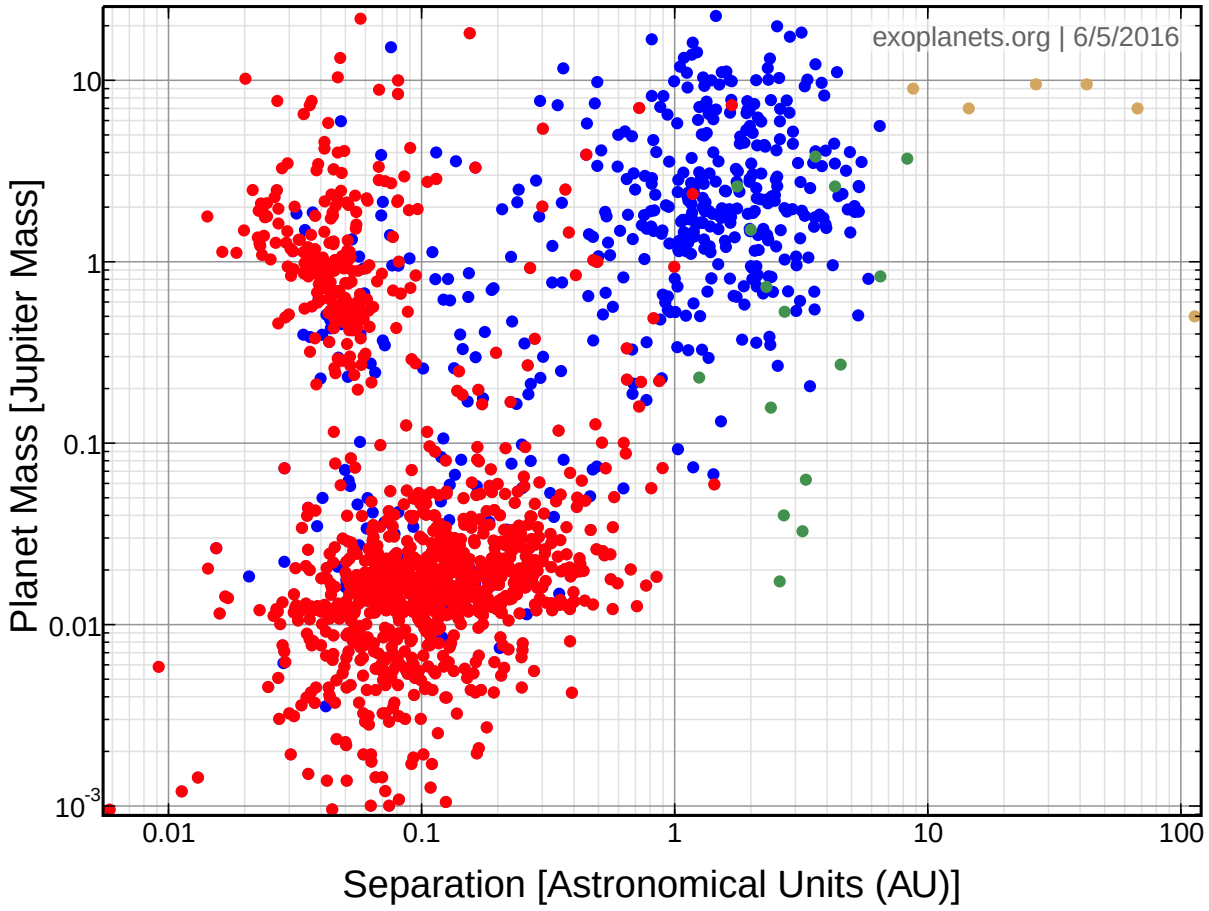

Figure 1.1 Summary of the mass-separation distribution for all confirmed exoplanets $\lesssim$13 M_J and $\lesssim$100 AU from the database, exoplanets.org [82], as of June 5, 2016. The red dots correspond to those detected with transit photometry, blue with radial velocity, green with gravitational microlensing and yellow with direct imaging.

Direct detection with high contrast imaging has found only a handful of planetary-mass companions so far. The primary factor behind this is the technical difficulty gaining sufficient signal-to-noise for objects many orders of magnitude dimmer than their bright parent stars at separations typically $<3''$. Because of this, all imaged planets are massive ($\sim$2–14 M_J) and in wide orbits ($\sim$10–2500 AU), and most are less than a few hundred Myr old. Being able to detect them directly requires them to be self-luminous, cooling as they shed off residual energy from their formation through gravitational contraction. Younger and more massive planets are brighter and easier to find. Even with its difficulties, direct imaging has the advantage of directly sampling the companion's light, enabling direct measurements of their brightnesses and colors. These values are independent constraints on formation, cooling, and compositional models. Brightness measurements at a number of different wavelengths can build up a low-resolution spectral energy distribution, which can clearly show the presence of molecules, clouds and hint at atmospheric mixing. Recent advances in adaptive optics and integral-field spectroscopy now enable moderate-resolution spectra to be taken directly; such as those of κ And b using the project 1640 integral-field spectrograph [92]. A detailed discussion of these

effects (molecules, clouds, mixing) and the constraints provided by spectra is given in Madhusudhan et al. [119]. All of these modeling efforts greatly benefit from the direct detection of the companion's photons with high contrast imaging.

The complementary nature of indirect and direct detections enables us to probe different regions of the mass-separation spectrum in Figure 1.1. While Jupiter is the most massive planet in our Solar System, one surprising discovery was that the tail at the high end of the mass distribution continues even beyond 10 M_J. The IAU loosely defines planets as being <13 M_J based on the masses necessary for deuterium and hydrogen burning, occurring around 13 M_J and 75 M_J respectively. Objects intermediate these two limits are termed 'brown dwarfs'. With a possible continuous mass distribution across 13 M_J, a formation-based distinction between brown dwarfs and planets might be desirable [34].

From the collection shown in Figure 1.1, we also now know that there is an abundance of giant planets on tight orbits, the 'hot Jupiters', along with many orbiting well outside the orbit of Neptune. Considering the canonical formation models for our Solar System [eg. 87, 109], giant planets are expected to form outside the frost line of the host star (at ∼3 AU for our Sun); other authors have shown that formation beyond 20 AU may be ineffective [91]. Therefore, where did the planets that we see today at such extreme separations form, and how did they arrive at their current positions? It is now widely believed that both populations formed between a few AU and a few tens of AU from their parent stars and then migrated through gravitational interactions with the protoplanetary disk, or with other giant companions [eg. 35, 105, 148].

With striking differences between most known exoplanets and our own Solar System, there are many questions about planet formation still to be answered. Some of the key scientific questions being addressed with recent instruments and surveys include:

- What are the 'bulk properties' of exoplanets (mass, radius, composition, orbital separation, density and age)?
- What are the dynamical evolutionary processes that led to the abundance of giant planets on tight orbits?
- How can we distinguish a giant planet from a very low mass brown dwarf, and how should we define the two classes of objects?
- How do systems containing multiple giant planets remain dynamically stable?

All of these questions require knowing either or both the planets' masses, obtained as a byproduct of orbit fitting, and the orbital elements themselves. The masses are necessary if the distinction between planets and brown dwarfs is to remain ∼13 M_J, while different formation channels may be effective over different mass ranges [eg. 34]. In addition, the models describing the initial formation conditions [eg. 125, 144, 174] all require an independently determined value of the companion's dynamical mass

to help break degeneracies between these different models and determine which can best explain the evolutionary path to the planet's current state. The orbital elements of an individual or an ensemble of planets are necessary for a number of exoplanet investigations. Knowing the semi-major axis can help to differentiate those that formed further out, which may have a higher likelihood of forming like stars through gravitational instabilities [eg. 192], from those closer in that may have formed via core-accretion [157]. The eccentricity component of the orbital elements is especially interesting for giant planets in non-circular orbits. Large eccentricities can indicate the planet is currently undergoing migration due to gravitational interactions with an outer unseen companion, by Kozai-Lidov oscillations [eg. 105, 113] or planet-planet scattering [eg. 35, 69]. These cases represent a small sampling of the scientific investigations where being able to solve for a planets' mass and orbital elements would be helpful.

Assuming the planets to obey Newtonian gravity, their orbits are described by Kepler's equations. A single form of observational data (astrometry or radial velocity) enables only a partial solution to the Keplerian model. A complete solution can be attained by combining radial velocity and direct imaging data for the same object. The TRENDS survey, which focused on revealing the origin of long (>10 yr) period trends in radial velocity surveys via direct imaging, took on this specific task for the case of binary stars and substellar companions [39, 41, 42, 43, 44]. The motivation for their work was to obtain the dynamic masses necessary to test theoretical models of low-mass companions. To accomplish this, they targeted nearby stars known to have strong radial velocity trends and performed high contrast direct imaging follow-up observations. While no companions in the planetary mass range were discovered, the general approach was validated.

With no open source software utilities to perform orbital fitting in 3-D with radial velocity and astrometry, I took it upon myself to develop one. The resulting package is entitled the Exoplanet Simple Orbit Fitting Toolbox (ExoSOFT); it fits any combination of radial velocity and/or astrometric data, and includes a collection of automated post-processing utilities to summarize the results. Provided both forms of data, it can accurately estimate the complete set of orbital parameters, including the dynamical mass of the companion to perform model verifications proposed by TRENDS. To make ExoSOFT more widely applicable, I designed it to work with either radial velocity or astrometric data on its own for cases where the companion has yet to be detected with the other. In these situations, even the partial solution ExoSOFT provides is capable of placing important constraints on the orbital eccentricity, period, inclination and lower mass limits, all vital to various exoplanet investigations. HR 8799 presents one especially pertinent case where only one form of data (astrometry) exists.

In Section 2.2 I outline the specific equations involved in the Keplerian models to predict the astrometric locations and radial velocities for a particular epoch given a complete set of orbital elements. Central to this are the well-vetted radial velocity equation (2.5) and Thiele-Innes method [184, 188]. The full joint model used in ExoSOFT involves at least 10 parameters, making it computationally difficult to sample the posterior probability distributions for each parameter with classic 'shotgun' Monte Carlo techniques. In Section 2.3, I cover the difficulties that may arise while trying to fit these

models and the techniques used by ExoSOFT to overcome them. I verified my implementation against simulated data of a Jupiter analogue, produced with an independent Keplerian model, in Section 2.4.

Following the verification of ExoSOFT, Chapter 3 presents its use in a study of the companion orbiting V450 Andromedae. A previous attempt to fit the orbit using radial velocity data alone produced an $m_2 \sin(i)$ value of 52 M_J, making the companion possibly sub-stellar [153]. My joint fitting to a broader coverage of radial velocity data and the first direct imaging detections of the companion independently constrain the inclination and find the companion to be a $0.282^{+0.042}_{-0.023}$ $M_\odot$ (295^{+44}_{-24} M_J) star on a nearly face-on, eccentric orbit. This result demonstrates the advantage of using multiple forms of data, to break model degeneracies and estimate a companion's dynamical mass directly.

A second application of ExoSOFT, to astrometry of the HR 8799 planetary system, is given in Chapter 4. This exciting system hosts four known planetary mass companions directly detected with high contrast imaging (HR 8799bcde; Marois et al. [127, 129]). As they are all in long period orbits (∼50–600 yrs) the orbital arcs measured so far cover a very small portion of the full orbits, complicating fitting efforts. One approach to simplifying this is to only consider face-on, circular and/or coplanar solutions. However, recent work by (eg. Konopacky et al. [104], Pueyo et al. [160], Zurlo et al. [200]) found that all three of those assumptions could be invalid for HR 8799 and indicated that the orbital plane of planet d might be inclined with respect to that of other three. To investigate their findings, I employ the MCMC capabilities of ExoSOFT to fit the self-consistent data set given in Konopacky et al. [104]. The posterior probability distributions produced by my MCMC analysis show all four planets are consistent with circular orbits, although that of planet c has an eccentricity of $e > 0.08$ at 68% confidence. Additionally, while the chains did not fully converge, I found evidence that the planets orbit about a common plane inclined by $35° \pm 4.4$, with mutual inclinations less than $\sim 5°$. These preliminary results suggest that the angular momentum vectors of all the major components of the system (planets, outer dust disk and star) approximately align.

The mass determination and multi-planetary system configuration discussions, in Chapters 3 and 4 respectively, demonstrate some of the important reasons to advance our measurement accuracies and the need to use multiple observables when possible. At only a couple decades old, the field of exoplanet observations is still young. Upcoming ground and space-based missions will dramatically expand the range of systems observed, many of which a joint orbital analysis with ExoSOFT will be possible.

The space-based telescope *Gaia* is the successor to the *Hipparcos* satellite, and is designed to perform accurate astrometry. A revised assessment in Perryman et al. [154] estimates *Gaia* will find ∼ 20,000 giant planets over its nominal 5 year mission, with a maximum on the order of 70,000 should it operate for its entire expected lifetime. With a peak sensitivity at ∼ 3.5 AU in semimajor axis, *Gaia* will provide important information to support investigations on the outer companions of systems also hosting hot Jupiters. Newly discovered exoplanets found with the improved astrometric accuracy of *Gaia* can be combined with follow-up observations using some of the upcoming ground-based extremely high precision radial velocity instruments. Many of these are on the way, with those expecting to

achieve first light over 2015-2017 including: NRES [57], CARMENES [161], HPF [120], IRD [181], MINERVA [179], ESPRESSO [152], EXPRES (co-PI's D. Fischer and C. Jurgenson), and SPIRou [6].

The combined observational capabilities of all the new ground and space-based facilities will shed light on some vital planetary formation questions, including: the ratio of gas giants to terrestrial planets, the dynamical influence they have on each other, the frequency of systems that contain both types of planets, the mass distribution of gas giants orbiting past the frost line and the frequency of Solar System analogues [64]. With these important questions to be soon investigated with the upcoming radial velocity and astrometric data, the benefits of ExoSOFT's open-source design and joint orbit fitting capabilities will continue to enhance its usefulness to the astronomical community.

Chapter 2

The Exoplanet Simple Orbit Fitting Toolbox

In this chapter I introduce the Exoplanet Simple Orbit Fitting Toolbox (ExoSOFT). This new open-source software suite is detailed here and utilized to attain the orbital parameters for the V450 And binary star system in Chapter 3 and for the HR 8799 multi-planet system in Chapter 4. In those respective chapters I discuss the implications and enhanced understanding of dynamical masses and orbital dynamics these improved parameter estimates enable.

This chapter is based on the paper:

Title: "The Exoplanet Simple Orbit Fitting Toolbox (ExoSOFT): An open-source tool for efficient fitting of astrometric and radial velocity data"

First Author: Kyle Mede

Status: At the time of this thesis' submission, the paper is under review for acceptance to The Astronomical Journal, with the application number #AAS00514.

Cite: (ExoSOFT; K. Mede & T. Brandt 2016, submitted)

Authorization to use the material from said paper has been included along with the submission of this thesis in accordance with the research ethics policies of The University of Tokyo.

2.1 Motivation to Develop ExoSOFT

Substellar companions exist in a wide array of masses and orbital configurations. Confirmed companions[1][2][3] have orbital separations ranging from 0.0044 AU to 2500 AU (for PSR 179-14 [8] and WD 0806-661B b [165] respectively), and masses as low as 0.022 $M_{\oplus}$ (PSR B1257+12 [194]). This broad spectrum has highlighted the somewhat arbitrary nature of mass-based categorizations. The canonical definition of a star is an object with sufficient core pressures for stable hydrogen burning, or a minimum mass of $\sim 73 - 89$ M_J depending on metallicity [33, 81]. An additional category of intermediate mass objects was long predicted and later supported with the discovery of GD 165 B [17] and Gliese 229 B [149]. These are now referred to as brown dwarfs, and loosely quantified as having a mass between ∼13–80 M_J where deuterium may burn in their cores, but not hydrogen. Lower mass companions are then called planets. Deuterium burning has a minimal effect on a brown dwarf's evolution; a more physically interesting distinction between brown dwarfs and planets might be their mechanism of formation [34].

Formation mechanisms are thought to be broken up into two general regimes: large objects form like stars, from the 'top down', while planets grow from the 'bottom up'. Stellar mass companions are believed to form early on through the cooling and contraction of a fragment of the primary's protostellar cloud, or slightly later from a fragment of its protoplanetary disk [20, 24, 29, 109, 192]. Giant planets are thought to form when a rocky planet becomes sufficiently massive to accrete gas directly from the circumstellar disk [75, 139, 157, 168]. In the case of core accretion, theoretical models predict bodies up through thousands of Earth masses, or tens of Jupiter masses [141], while Kratter et al. [106] showed that gravitational instabilities could, under certain conditions, produce the ∼10 M_J companions orbiting HR 8799 [127, 129]. In fact, "the minimum Jeans mass, or when fragmentation must stop" was found forty years ago to be ∼7 M_J in Low & Lynden-Bell [116], with even lower masses possible when other physical effects (e.g. magnetic fields) are taken into account [14, 15]. Thus, the ranges of companion masses possible in the two formation mechanisms are likely to overlap.

When investigating the formation and dynamical evolution of sub-stellar companions, the value of their separation and eccentricity can prove useful. Simply considering the local environment of our Solar System, planetary evolution models [eg. 87, 109] suggest gas giants should dwell in stable orbits outside the frost line of their host star. Interestingly though, the results of exoplanet surveys using the transit [eg. 10, 13, 156] and radial velocity techniques [eg. 21, 45] show a large number of gas giants reside in tight orbits, the so-called 'hot Jupiters', clearly contesting these simple evolutionary models. Hot Jupiters are now thought to have formed further out and migrated inward due to the gravitational interactions with an outer companion or the disk, though there have been suggestions that they can form in-situ [49, 94]. Two such migration mechanisms when a companion is involved are planet-planet

[1] http://exoplanet.eu
[2] http://exoplanets.org/
[3] http://exoplanetarchive.ipac.caltech.edu/

scattering [35, 69], and Kozai-Lidov oscillations [105, 113], [eg. 147, 148]. In both cases, the outer companion is expected to be more massive and in a highly elliptical orbit. For planets in wide orbits, formation in-situ through core accretion may be ineffective beyond 20 AU [91]. If those in the HR 8799 system were formed inside this distance and migrated out to their current positions through strong planet-planet scattering, it could have excited their eccentricities [51]. However, dynamical models show that the system is likely unstable for all but a limited range of nearly circular orbits [eg. 62, 69, 76].

The importance of the parameters describing a companion's orbit, including the mass, eccentricity and separation, supports the use of multiple observation types to further enhance the constraints on their values. Two of the commonly applied observing techniques for detecting sub-stellar companions are the radial velocity method and high-contrast direct imaging. From those, the measured radial velocity and astrometry can be simultaneously fit with Keplerian models to solve for the orbital elements. Solutions found in this manner are capable of measuring the companion's dynamical mass, rather than the $m_2 \sin(i)$ value estimated with the RV method alone. Thus, the $\sin(i)$ degeneracy may be broken, enabling separate constraints on the inclination and companion mass. Deitrick et al. [50] and McArthur et al. [133] employed a version of this method for the υ And system. Although the companions were not directly detected, the relative astrometry of the host star allowed them to show the masses of the outer two planets were a factor of 2–4 higher than the lower limits from purely radial velocity data. Interestingly, they also found those companions to be orbiting in different planes, with inclinations differing by $\sim$14°.

Tightly constrained values for a companion's dynamical mass are key to probing atmospheric models and to describing the object's formation conditions. The atmospheric models of brown dwarfs and low-mass stars require input parameters that are often degenerate with one another, including effective temperature, age, metallicity, radius and mass [12]. To help break the degeneracies in these atmospheric models, measurements of the physical properties, such as dynamical mass, independent of spectra or photometry, are required [40]. The initial conditions of the sub-stellar object are a crucial component to differentiate between the formation mechanisms and subsequent evolution of giant planets. These have been put into broad classes, such as the 'hot start' [eg. 2, 108, 144], 'cold start' [125], or an intermediate 'warm start' [174]. Similar to the atmospheric models of objects that form like stars, accurate estimates of the age and dynamical mass can break the degeneracies and help investigate which best explains how the object came to its current state.

Of the nearly 3300 confirmed exoplanets[4], $\sim$600 were found through radial velocity measurements and $\sim$40 with direct imaging, although none have data of both forms. While a small number of objects with simultaneous coverage and estimated dynamical masses exist, they are all in the low-mass star and high mass brown dwarf range [i.e. 39, 41, 42, 43, 44, 166, also: J. Hagelberg et al. 2016, in preparation]. Given the uncertainties in the atmospheric models of exoplanets and low-mass brown dwarfs, and the variety of orbital evolution scenarios, accurate dynamical mass values are important.

[4] http://exoplanetarchive.ipac.caltech.edu/

The advancements in ground and space-based instrumentation will further populate the lists of known low mass companions observed with both techniques. With *Gaia* precisely measuring acceleration in the plane of the sky for $\sim 10^9$ stars, it is expected to lead to the discovery of thousands of planets astrometrically. In addition, high-dispersion spectrographs such as IRD [181], CRIRES [100] and SPIRou [5], will measure the radial velocity of low-mass stars with poor or no orbital coverage from previous instruments. For those systems with separations and predicted contrasts detectable with next generation integral field spectrographs, including CHARIS [155], SPHERE [38], and GPI [118], follow-up observations can help investigate their atmospheres. The higher sensitivities of all these instruments and spacecraft will increase the number of known companions and expand the overlap range of those detectable in both the radial velocity and astrometric data.

In this chapter I introduce a new, open-source software package, ExoSOFT, for performing joint fitting of a system's orbital elements. The chapter is organized as follows. Section 2.2 covers the joint 3-dimensional model used, the background on fitting models of this kind and the approach ExoSOFT utilizes in Section 2.3, and the implementation and verification of its capabilities for a synthetic example system in Section 2.4.

2.2 Modeling the Orbit

The classical solution to the two-body problem in Newtonian gravity is given by using Kepler's laws; six parameters are needed to fully describe the orbits (eg. Heintz [89]). I implement this approach adding some intermediate parameters to facilitate the calculation and comparison to measured radial velocity and astrometry. The full set of parameters is given in the top section of Table 2.1; these are used to calculate the additional parameters in its lower section. The angular orbital elements defining the orientation of the orbit relative to the plane of the sky and true north are shown for the companion's orbit in Figure 2.1.

The predicted radial velocity and astrometry values, to be compared to the measured data for epoch t, are calculated in the following way. The equations for the projected line-of-sight velocity, or radial velocity v, and projected locations in the plane of the sky, the astrometry, both require the anomalies M, E and θ. Thus, the anomalies are determined first, followed by v, ending with the Thiele-Innes equations to get relative right ascension, $\Delta\alpha$ and declination, $\Delta\delta$.

The Eccentric Anomaly E and True Anomaly θ are found starting from the Mean Anomaly M

$$M = \frac{2\pi}{P}\,(t - T_o) \tag{2.1}$$

and its relation to E through Kepler's equation is

$$M = E - e \times \sin(E), \tag{2.2}$$

Table 2.1. Model Parameters

Symbol	Parameter
ϖ	Parallax
P	Orbital period
m_1	Mass of the primary star
m_2	Mass of the companion
Ω	Longitude of the Ascending Node
ω	Argument of Periapsis
i	Inclination
e	Eccentricity
T_o	Time of Last Periapsis
γ	Instrument velocity offset
$m_{\rm tot}$	Total mass $(m_1 + m_2)$
$a_{\rm tot}$	Total semi-major axis $(a_1 + a_2)$
θ	True Anomaly
E	Eccentric Anomaly
M	Mean Anomaly
K	Radial Velocity Semi Amplitude

where e is the eccentricity. I solve Equation (2.2) with Newton's method and use the resulting value to calculate θ following

$$\theta' = \cos^{-1}\left(\frac{\cos(E) - e}{1 - e \times \cos(E)}\right) \tag{2.3}$$

and

$$\theta = \begin{cases} \theta' & E \leq \pi \\ 2\pi - \theta' & E > \pi \end{cases} . \tag{2.4}$$

Equations (2.2)-(2.4) provide the two key time dependent values, E and θ.

The radial velocity as measured for the primary due to the companion's motion is

$$v(t) = K_1 \left[\cos(\theta(t) + \omega_1) + e\cos(\omega_1)\right] + \gamma \tag{2.5}$$

where ω_1 is the Argument of Periapsis for the primary, γ is the instrument velocity offset and the semi amplitude of the primary (K_1) is

$$K_1 = \left[\frac{2\pi G}{P}\right]^{1/3} \frac{m_2 \sin(i)}{(m_{\rm tot})^{2/3}} \frac{1}{\sqrt{1 - e^2}} \tag{2.6}$$

with m_2 being the companion's mass, $m_{\rm tot}$ the total mass of both objects and P the period. When only radial velocity data are available, Equation (2.6) shows that the companion's mass and inclination cannot be independently constrained.

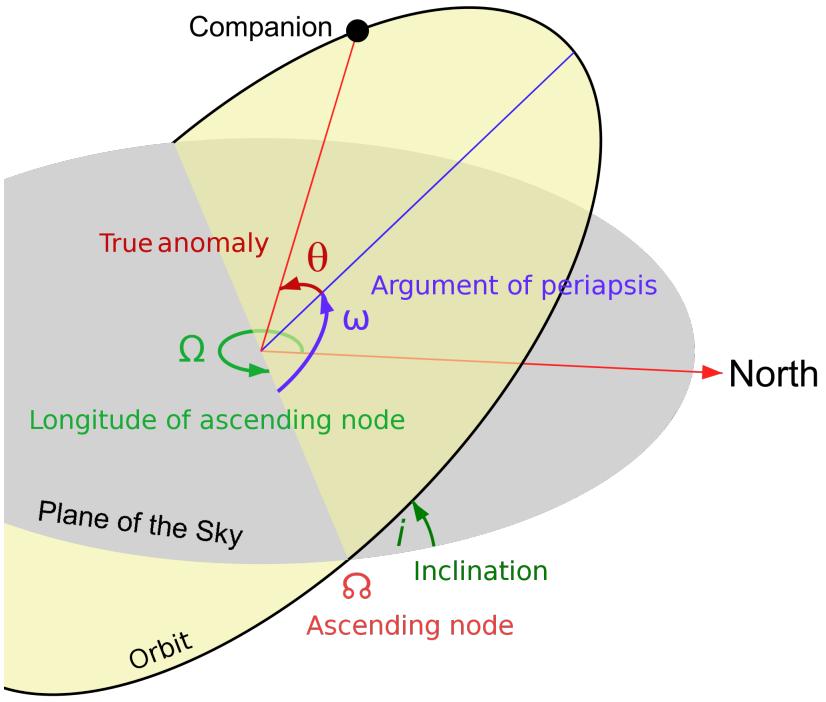

Figure 2.1 Configuration of the companion's orbit in 3-dimensional space. The three angular orbital elements ω, Ω and i orient the companion's orbit with respect to the plane of the sky and true North.

The Thiele-Innes method allows for quick computation of the predicted astrometric values given a set of input orbital elements [184, 188], using a set of intermediate quantities

$$A = a_{\rm tot}\left[\cos(\Omega_2)\cos(\omega_2) - \sin(\Omega_2)\sin(\omega_2)\cos(i)\right] \tag{2.7}$$

$$B = a_{\rm tot}\left[\sin(\Omega_2)\cos(\omega_2) + \cos(\Omega_2)\sin(\omega_2)\cos(i)\right] \tag{2.8}$$

$$F = a_{\rm tot}\left[-\cos(\Omega_2)\sin(\omega_2) - \sin(\Omega_2)\cos(\omega_2)\cos(i)\right] \tag{2.9}$$

$$G = a_{\rm tot}\left[-\sin(\Omega_2)\sin(\omega_2) + \cos(\Omega_2)\cos(\omega_2)\cos(i)\right]. \tag{2.10}$$

In Equations (2.7)-(2.10), the total semi-major axis of the apparent ellipse ($a_{\rm tot}$) is calculated with Kepler's third law,

$$a_{\rm tot} = \left[\frac{P^2 G m_{\rm tot}}{4\pi^2}\right]^{1/3} \tag{2.11}$$

with G in Equation (2.11) being Newton's gravitational constant.

Equations (2.7)-(2.10) give the relative location of the secondary with respect to the primary in the plane of the sky. The matching relative right ascension $\Delta\alpha$ and declination $\Delta\delta$ for comparison to the data are found with

$$\Delta\delta = AX(t) + FY(t) \tag{2.12}$$

$$\Delta\alpha = BX(t) + GY(t) \tag{2.13}$$

given

$$X(t) = \cos(E(t)) - e \tag{2.14}$$

$$Y(t) = \sqrt{1 - e^2}\sin(E(t)) \tag{2.15}$$

where G in Equation (2.13) refers to the Thiele-Innes G (Equation (2.10)).

The orbits of the two bodies m_1 and m_2 have matching values for all the orbital elements except Ω and ω. To convert between them, the relations $\omega_1 = \omega_2 + \pi$ and $\Omega_1 = \Omega_2 + \pi$ are used. For all cases, I assume the measured astrometry to be the relative positions of the two bodies tracing out an apparent ellipse on the sky, which reduces to the orbit of the companion when $m_1 \gg m_2$.

The equations in this section calculate a set of observables (v, $\Delta\alpha$, and $\Delta\delta$) that are then compared to the corresponding measurements.

2.3 Model Fitting

2.3.1 Method

Model fitting can be broken down into two main tasks: solving for a set of parameters approaching the best fit, and estimating their uncertainties. In a Bayesian framework the full set of information is contained within the posterior probability distribution of the model parameters, $p(\text{Model}|\text{Data})$. Ford [67] & Ford [68] discuss the use of Bayesian inference to solve for this distribution in the case of fitting observations of exoplanets to Keplerian models; for details beyond those given here, we refer the reader to those papers.

The posterior probability distribution, $p(\text{Model}|\text{Data})$, is computed using Bayes' theorem,

$$p(\text{Model}|\text{Data}) \propto p(\text{Data}|\text{Model})p(\text{Model}). \tag{2.16}$$

Here $p(\text{Data}|\text{Model})$ is the likelihood of the model parameters, $\mathscr{L}(\text{Model})$, and $p(\text{Model})$ is the prior probability of the parameters based on previous knowledge. Assuming that the errors in the observed data are independent and Gaussian distributed, the likelihood can be expressed in terms of the usual χ^2:

$$\mathscr{L}(\text{Model}) = p(\text{Data}|\text{Model}) = \exp\left(-\frac{\chi^2}{2}\right) \tag{2.17}$$

with χ^2 being a sum over data points i,

$$\chi^2 = \sum_i \frac{(\text{Model}_i - \text{Data}_i)^2}{\sigma_i^2} \tag{2.18}$$

The posterior probability distribution can then be computed by finding the value of $\mathscr{L}(\text{Model})p(\text{Model})$ for all possible parameter combinations and integrating. Due to the high dimensionality of Keplerian models though, the parameter space is large, making this brute-force approach computationally problematic. A variety of routines exist for sufficiently sampling the posterior without calculating its value everywhere. In Section 2.3.2 I will discuss the approaches used in ExoSOFT, particularly that of Markov Chain Monte Carlo, along with the specific priors for each of the model parameters.

2.3.2 MCMC

Forming the posterior distributions can be achieved by integrating Bayes' theorem over the model's parameter space. Depending on the form of the likelihood function and the dimensionality of the model space, evaluating this integral directly or through 'shotgun' Monte Carlo can prove computationally impractical. One alternative is to draw statistically dependent samples with Markov Chain Monte Carlo (MCMC) [114]. A Markov Chain is a sequence of points satisfying the dependency defined by the Markov property: each point in the chain is a function only of its immediate predecessor with no memory of the chain history. MCMC guarantees convergence to the posterior probability distributions in the limit of a large number of steps. A widely used algorithm to form such chains is that of Metropolis-Hastings, originally detailed in Metropolis et al. [138] and further generalized by Hastings [85]. Unfortunately, the convergence rate is typically impossible to compute; convergence is discussed in more detail in Section 2.3.3.

The Markov process in Metropolis et al. [138] enables the drawing of samples from an unknown target distribution of interest, $\Pi(\boldsymbol{\xi})$. Its algorithm is based on drawing "unbiased perturbations" of the current step's parameter values to form a proposed step. These steps are always accepted if they improve the likelihood, and sometimes accepted otherwise. The probability of accepting a step that reduces the likelihood is given by the rejection function,

$$r\left(\boldsymbol{\xi}, \boldsymbol{\xi}_{j+1}\right) = min\left\{1, \frac{\Pi\left(\boldsymbol{\xi}_{j+1}\right)}{\Pi\left(\boldsymbol{\xi}_{j}\right)}\right\}. \tag{2.19}$$

For each proposed step, a random number α is drawn from $U[0,1]$. If $\alpha \leq r\left(\boldsymbol{\xi}, \boldsymbol{\xi}_{j+1}\right)$, the proposed step is accepted as the next step in the chain, while if α is larger than the rejection function, the chain remains at its current location. With the target distribution of interest in this case being the posterior probability distribution, the ratio $\Pi\left(\boldsymbol{\xi}_{j+1}\right)/\Pi\left(\boldsymbol{\xi}_{j}\right)$ becomes

$$\frac{p\left(Model_{j+1}|Data\right)}{p\left(Model_{j}|Data\right)} = \frac{\mathscr{L}\left(\boldsymbol{\xi}_{j+1}\right)}{\mathscr{L}\left(\boldsymbol{\xi}_{j}\right)}\frac{p\left(\boldsymbol{\xi}_{j+1}\right)}{p\left(\boldsymbol{\xi}_{j}\right)}, \tag{2.20}$$

where $p\left(\boldsymbol{\xi}_{j+1}\right)/p\left(\boldsymbol{\xi}_{j}\right)$ is the ratio of the prior probabilities of the proposed and current models. Putting these together gives the form of the rejection function used in ExoSOFT,

$$r\left(\boldsymbol{\xi}, \boldsymbol{\xi}_{j+1}\right) = min\left\{1, \frac{\mathscr{L}\left(\boldsymbol{\xi}_{j+1}\right)}{\mathscr{L}\left(\boldsymbol{\xi}_{j}\right)}\frac{p\left(\boldsymbol{\xi}_{j+1}\right)}{p\left(\boldsymbol{\xi}_{j}\right)}\right\}. \tag{2.21}$$

One element of the algorithm's generalization in Hastings [85] was to include the ratio of the proposal distributions, $\tau\left(\boldsymbol{\xi}_{j+1}, \boldsymbol{\xi}\right)/\tau\left(\boldsymbol{\xi}_{j}, \boldsymbol{\xi}_{j+1}\right)$. This compensates for the "flow bias" that would arise if drawing proposed samples from asymmetric distributions [114]. I opt for the simpler form in Metropolis et al. [138] that strictly requires the proposal distributions to be symmetric, i.e., the probability of a proposed step from $\boldsymbol{\xi}_1$ to $\boldsymbol{\xi}_2$ is the same as from $\boldsymbol{\xi}_2$ to $\boldsymbol{\xi}_1$. Specifically, ExoSOFT uses uniform distributions of fixed width in each parameter centered on the current step. Another popular symmetric choice is a normal distribution.

Following the Gaussian error assumption in Section 2.3.1, the likelihood ratio is

$$\frac{\mathscr{L}\left(\boldsymbol{\xi}_{j+1}\right)}{\mathscr{L}\left(\boldsymbol{\xi}_{j}\right)} = \exp\left(-\frac{\chi^2_{\boldsymbol{\xi}_{j+1}} - \chi^2_{\boldsymbol{\xi}_{j}}}{2}\right). \tag{2.22}$$

The prior probabilities, or 'priors', for each parameter are chosen with simplicity in mind. These should only be considered as suggestions, and may be easily changed in the ExoSOFT settings files to suite the user's preferences or to take into account the results of more recent work. The complete set of parameters in the full joint analysis are (m_1,m_2,ϖ,P,i,e,T_o,Ω,ω,γ). The priors are given periodic boundary conditions where appropriate, allowing Ω and ω to be drawn without limits, but the stored values are then shifted into [0,2π].

For m_1, the prior can be represented by the Initial Mass Function (IMF) or Present Day Mass Function (PDMF). Chabrier [31] found functional forms of these for a range of stellar populations, including those of the galactic disk. For m_2 however, particularly for stellar binaries, the IMF may be a poor approximation to the companion mass function (CMF); that of Metchev & Hillenbrand [136] might be more appropriate. More recent investigations [e.g. 28] were consistent with Metchev & Hillenbrand [136] down to a few Jupiter masses. The PDMF and IMF can be found in table 1 of Chabrier [31], and that of the CMF in equation 8 of Metchev & Hillenbrand [136]. By default ExoSOFT uses the PDMF for primary and CMF for the companion, with the IMF being an option also available to the user for either body.

The prior for the parallax (ϖ) may be derived from the assumption that stars are uniformly distributed in space. For nearby objects, under a few 100 pc, this prior is

$$p\left(\varpi\right) \propto \frac{1}{\varpi^4}. \tag{2.23}$$

In cases where high S/N distance measurements are available, this information can be included with a Gaussian prior with center and width equal to its distance and error, respectively. These two components would then be multiplied to form a combined prior for the parallax. For distant objects, over a few hundred pc, the assumption of uniform stellar distribution is invalid. Low S/N measurements of the parallax, in combination with Equation (2.23), would lead to unrealistically large distances. ExoSOFT currently requires accurately measured parallaxes. In practice, these are available for nearby

bright stars from *Hipparcos* [189], and the sample of objects with well-measured parallaxes will soon expand dramatically thanks to *Gaia*.

The period is given a logarithmic prior,

$$p\left(P\right) \propto \frac{1}{P} \tag{2.24}$$

and systems are assumed to be randomly oriented with:

$$p\left(i\right) \propto \sin(i) \tag{2.25}$$

To accommodate the range of possible formation histories and system types, ExoSOFT adopts two different priors for the eccentricity. From a theoretical perspective, Ambartsumian [3] found that if stellar orbits are distributed based on the equipartition theorem, then $p(e) \propto e$. This was later supported by observations of long period binary stars (P >1000 days) in Duquennoy & Mayor [54]. For exoplanets, a variety of mechanisms exist by which high eccentricities could be damped or excited (eg. disk-planet interaction, planet-planet scattering). Jurić & Tremaine [99] showed that planet-planet scattering could produce roughly a Rayleigh distribution with a $\sigma \sim 0.3$, while a uniform distribution over $e \in U[0, 0.8]$ was suggested in Cumming et al. [45]. ExoSOFT currently allows for two priors, $p(e) \propto e$ and $e \in U[0, 0.98]$.

The remainder of the parameters, (T_0, Ω, ω, γ), have been given uniform priors.

2.3.3 Optimization

Given an infinitely long Markov chain, convergence to the posterior probability distributions is guaranteed. In practice though, when trying to integrate Bayes' theorem for a particular model, one of the primary goals is to minimize the number of samples necessary to achieve sufficient convergence. Therefore, before performing MCMC, a metric to measure its convergence is required along with steps to optimize the convergence rate.

It is difficult to determine if a Markov Chain has converged to the posterior probability distribution. From a given set of parameter values, there is no guarantee that the likelihood function will smoothly increase towards the global maximum of the posterior. In cases with complicated likelihood topography, there might be many places where a chain could become stuck. Chains started near a local maximum could falsely appear to have converged or take a long time to diffuse into other regions. For this reason, the specific starting position of a Markov chain, and any following samples drawn far from the likelihood peaks, must be removed to avoid any disproportionalities in the posterior distributions they might induce. This initial period is referred to as the 'burn-in'. While the exact number of steps involved is not clearly defined, Tegmark et al. [182] took it to be over when the likelihood in a particular chain was equal to the median likelihood of all chains combined.

The rate at which a Markov chain explores the posteriors is related to the width, or σ, of each parameter's proposal distribution (τ). For large σ, proposed steps tend to lie far from the current one and in a region where they are unlikely to be accepted. By contrast, a small σ would lead to a high rate of acceptance, but a slow rate at which the posteriors are explored. Gelman et al. [73] showed that the highest diffusion speed of a one dimensional model was achieved when the probability of accepting a proposed step was 0.441. They tested a variety of multi-dimensional models concluding that an acceptance rate of ∼25% is suitable for higher dimensional models and ∼50% for those with only 1 or 2 dimensions.

With a Markov sampling scheme the dependence between neighboring samples can dramatically reduce the number of effectively independent steps taken. Unfortunately, prior to running a Markov chain, there are no direct methods to predict how many independent steps will be taken over a certain number of samples. Instead, following the completion of all Markov chains, a common practice is to estimate if enough steps were taken using the Gelman-Rubin statistic, $\widehat{R}$. This popular metric for assessing the level of convergence to the posterior probability distributions is described in Ford [68] and originally formulated in Gelman & Rubin [74]. It is calculated for each model parameter individually, with the key elements of its formulae being the parameter's variance within a chain, $W(z)$, and that between the chains, $B(z)$. In Equations (2.26)-(2.29) there are N_c Markov chains, each of length L_c. With this, the equations are

$$W\left(z\right) = \frac{1}{N_c}\sum_{c=1}^{N_c}\frac{1}{L_c-1}\sum_{i=1}^{L_c}\left(z_{ic}-\overline{z}_{.c}\right)^2 \tag{2.26}$$

$$B\left(z\right) = \frac{L_c}{N_c-1}\sum_{c=1}^{N_c}\left(\overline{z}_{.c}-\overline{z}_{..}\right)^2 \tag{2.27}$$

where $\overline{z}_{.c}$ represents the the mean value of model parameter z over chain c, and $\overline{z}_{..}$ is its mean over all chains. Then,

$$\widehat{R}\left(z\right) = \sqrt{\frac{\widehat{var}^{+}\left(z\right)}{W\left(z\right)}} \tag{2.28}$$

given,

$$\widehat{var}^{+}\left(z\right) = \frac{L_c-1}{L_c}W\left(z\right) + \frac{1}{L_c}B\left(z\right). \tag{2.29}$$

Values of $\widehat{R}$ ≤1.01 imply convergence to the final posterior probability distribution with a precision of 1%.

The burn-in and sampling are handled as follows. To minimize the burn-in, suitable starting positions for the Markov chains are found using Simulated Annealing. As discussed in Kirkpatrick et al. [103], Simulated Annealing also makes use of the Metropolis-Hastings algorithm with an additional

'temperature' factor in the likelihoods ratio, modifying this ratio in the rejection function to

$$\left(\frac{\mathscr{L}\left(\boldsymbol{\xi}_{j+1}\right)}{\mathscr{L}\left(\boldsymbol{\xi}_{j}\right)}\right)^{1/T} = \exp\left(-\frac{\chi^2_{\boldsymbol{\xi}_{j+1}} - \chi^2_{\boldsymbol{\xi}_{j}}}{2T}\right). \tag{2.30}$$

At high temperatures Equation (2.30) is temperature dominated, and likely to accept even unfavorable steps, thereby mitigating any local topographical bumps encountered. A cooling scheme started at a sufficiently high temperature ($\gtrapprox 100$) can then explore a large portion of the parameter space and be slowly 'annealed' towards the global best fit. After this, I use a version of the Metropolis-Hastings algorithm to determine the appropriate widths for each proposal distribution. Periodically the acceptance is calculated and σ values adjusted accordingly until stable acceptance rates between 25-35% are reached; this process is occasionally referred to as Sigma Tuning. Lastly, trial runs are used to estimate the number of total samples necessary to achieve sufficient convergence, as indicated by $\widehat{R}\leq 1.01$.

2.4 Implementation

In the following subsections I describe how the model discussed in Section 2.2 and types of parameter space exploration in Section 2.3 are implemented. The bulk of the code was written in the Python programming language, with the more computationally expensive model in C++ and interfaced using SWIG. Implementing the model in this way makes it run 10-60 times faster than the same code written purely in Python. ExoSOFT can be found for public download at https://github.com/kylemede/ExoSOFT.

2.4.1 Simulation Stages

ExoSOFT offers four algorithms for exploring the parameter space each for a different task, standard 'shotgun' Monte Carlo, Simulated Annealing, Sigma Tuning and MCMC.

As discussed in Section 2.3.2, standard Monte Carlo is suitable for models with few free parameters, or when the likelihood function is not strongly peaked. In such cases, it could in fact sample the posterior probability distributions significantly faster than MCMC. With each sample being completely independent, it can also be useful for getting an idea of where the regions of minimum χ^2 lie.

In cases where standard Monte Carlo is inefficient, I suggest a three stage progression through the parameter space, as outlined in Section 2.3.3: Simulated Annealing to find parameters near the global minimum, Sigma Tuning to find the step sizes for efficient sampling, and lastly MCMC to fill out the posterior probability distributions.

My implementation of Simulated Annealing follows the typical process discussed in Section 2.3.3. The chains are repeatedly heated and cooled, each time from a lower starting temperature, while

maintaining a list of the best fits achieved so far. This process is stopped when the fits have all converged to a single set of parameter peaks in the posterior probability distributions.

2.4.2 Verification

The model was verified with synthetic data produced using an independent Keplerian tool built upon the PyAstronomy package [5]. The observable values had their errors realized from Gaussian distributions, using a percentage of each observable's absolute mean as the distribution widths. Such synthetic data were produced for various systems spanning the range of exoplanets and binary star systems observed to date to ensure ExoSOFT's ability to fit any system of interest.

For demonstration purposes, the approximate orbital elements of Jupiter were used assuming a host star at a distance of 20 pc, or a parallax of 50 mas, with the orbital plane inclined by 45° to Earth's line-of-sight. A variety of measurement errors were assumed for the same orbital elements to show the convergence of the resulting posterior distributions with improving data quality; the errors indicated are a percentage of each observable parameter's absolute mean value.

Figure 2.2 shows the posteriors using realizations of 10%, 5% and 1% Gaussian noise on the measured parallax, radial velocity, relative right ascension and relative declination. The 68% confidence regions shrink by a factor of ∼10 from the 10% to 1% cases, shown as the green and red lines in Figure 2.2 respectively. The posterior distributions of T_0 and ω (not shown) have larger widths and decrease faster with improving data quality; this is an artifact of my choice of a nearly circular orbit. In all of the hypothetical Jupiter demonstration cases, ExoSOFT used a uniform prior for e, appropriate for planets. This was implemented by drawing ω and e simultaneously according to the parametrization from Albrecht et al. [1].

Figure 2.3 shows the resulting posteriors for one realization of 5% measurement errors; Table 2.2 provides a complete summary of the fit values. The best-fit orbit has $\chi^2 = 46.8$ for 35 degrees of freedom (25 epochs of radial velocity data, 10 epochs of astrometry in RA and Dec, and 10 fitted parameters), for a reduced $\chi^2 = 1.33$. Figure 2.4 shows the best-fit orbit plotted along with the noisy astrometry and radial velocity data. The residuals, as expected, scatter about the best-fit orbit and typically lie within $\sim 1\sigma$ of the median.

The joint model given in Section 2.2 mutually constrains the parameters P, $m_{\rm tot}$, ω^*, i, e and T_0, where ω^* represents the value for either body following the relation $\omega_1 = \omega_2 + \pi$. The other parameters ($\gamma$, m_2, Ω_2, ϖ) are constrained by a single observation type, or in the form of a combined parameter, as is the case for $m_{\rm tot} = m_1 + m_2$. I investigated the mixing and convergence of each parameter by calculating the number of effective steps and the Gelman-Rubin statistic. The number of effective steps was estimated following its definition in Tegmark et al. [182]: the total number of steps divided by correlation length, where the correlation length is the number of steps necessary to achieve a variance

[5] Found at https://github.com/sczesla/PyAstronomy

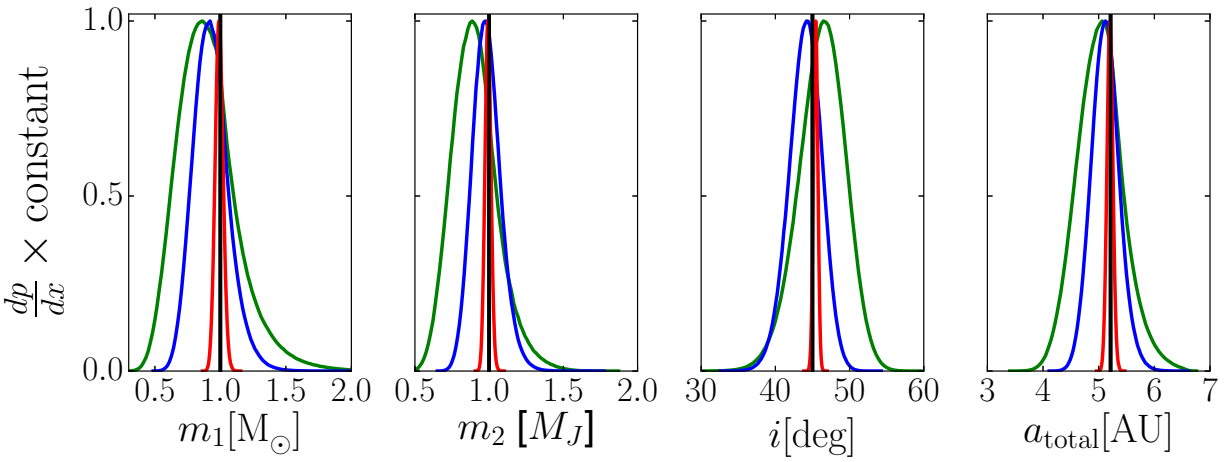

Figure 2.2 The convergence of ExoSOFT's posterior probability distributions to noisy synthetic data. The observational errors in astrometry and radial velocity are assumed to be a percentage of the absolute mean value for each observable ($\Delta\delta$, $\Delta\alpha$, v). I draw a realization of the noise for each measurement from a normalized Gaussian of given width. The lines shown are for 10, 5 and 1% errors, corresponding to the colors green, blue and red. The assumed true values are indicated with black vertical lines.

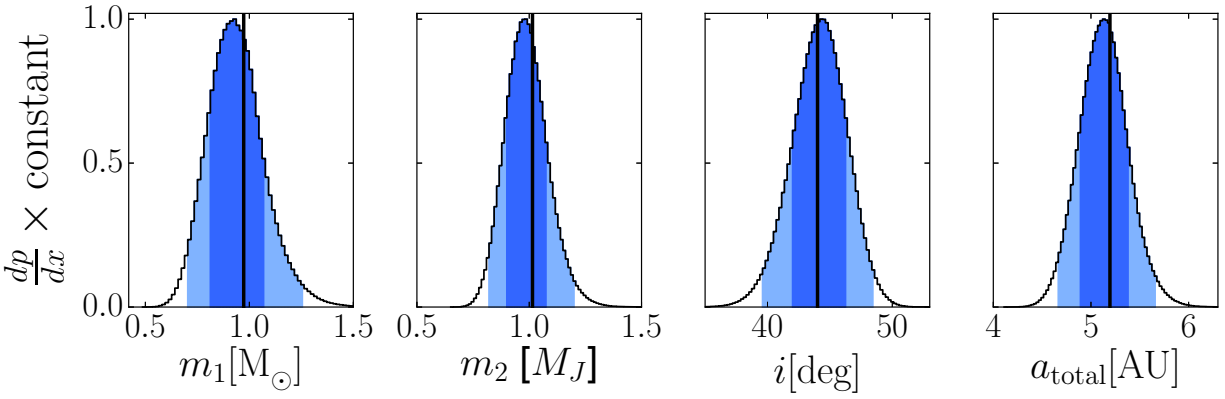

Figure 2.3 Posterior probability distributions for a subset of the parameters fit during verification with synthetic data of a Jupiter analogue with a 5% realization of the errors in radial velocity and astrometry, at distance of 20 pc and inclination of 45°. The darker blue represents the 68% regions of confidence around the medians, with the lighter being that of 95% confidence. As expected, the vertical black lines representing the true values fall within our 68% confidence regions.

equal to half that of the entire chain. I compute the number of effective steps for each parameter. With 7 parallel chains, each 5×10^7 samples long, all the parameters met the $\widehat{R}$ <1.01 convergence criterion, with T_0 being the least convergent in all three error realizations. For the 5% case, it only took 636 effective steps and had $\widehat{R}$=1.003. This slow convergence is an artifact of the choice to use a nearly circular orbit (the definition of T_0 is arbitrary for a circular orbit) and is much less pronounced for more eccentric systems.

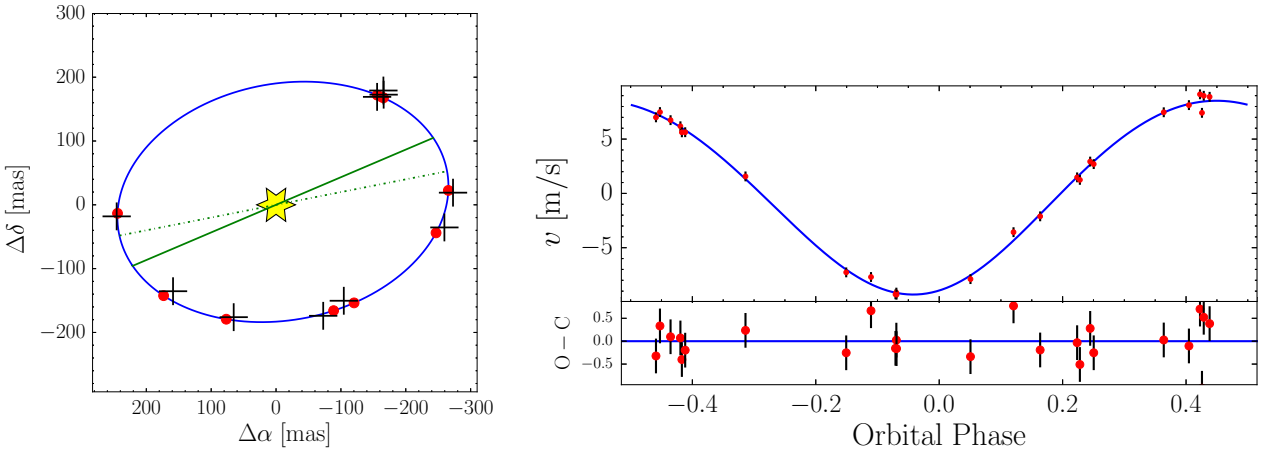

Figure 2.4 The best-fit orbit plotted atop the synthetic astrometry (left) and radial velocity data (right) of our Jupiter analogue test case with a 5% realization of the errors. In the astrometry fit the solid green line represents the projected semi-major axis and the dash-dot the line of nodes. The red dots represent the predicted location and radial velocity values at the time of each observation.

Table 2.2. Synthetic Jupiter Fit Results

Parameter	Synthetic	Best-Fit	Median	1σ Range
m_1 $[M_\odot]$	1	0.97	0.93	0.13
m_2 $[M_J]$	1	1.015	0.984	0.093
ϖ [mas]	50	49.6	50.3	2.3
Ω_2 [°]	100.6	101.3	101.7	1.1
e	0.048	0.046	0.043	0.014
T_0 [MJD]	50639	50660	50650	140
P [Yrs]	11.9	12.00	12.03	0.18
$a_{\rm tot}$ [AU]	5.21	5.19	5.13	0.25
i [°]	45	44.0	44.2	2.2
ω_2 [°]	14.8	17	16	12
γ [m/s]	0	−0.03	−0.05	0.16
χ^2 (ν)	46.8 (35)			

While this test case is at the edge of current instruments' sensitivity, the $\sim 0\farcs2$ separation is within the expected limits of upcoming instruments like CHARIS [155], SPHERE [38] and GPI [118]. However, even with the improved contrast ratios expected at these separations, this hypothetical planetary system would need to be dramatically younger than Jupiter for detection through direct imaging techniques. The uncertainties in m_1 and m_2 also depend on the precision of the measured parallax, though this is already better than 1% for many bright, nearby stars [189] and will further improve with the forthcoming *Gaia* data release.

An example of ExoSOFT applied to real data can be found in Hełminiak et al. [90], a summary of which is given in Chapter 3 of this thesis. In that paper we introduce the first direct imaging detections of the companion to V450 And, and solve for its joint orbital solution. The full set of orbital elements

were able to break the $\sin(i)$ degeneracies of earlier fitting attempts and show the companion to in fact be a low-mass star, instead of sub-stellar as previously estimated. A further example of its use includes that to the astrometry of the multi-planet system orbiting HR 8799, discussed in Chapter 4. By utilizing the self-consistent astrometry from the Keck Observatory and the MCMC capabilities of ExoSOFT, I found preliminary evidence that the planets may orbit about a common plane with a similar inclination to the other major orbiting components in the system.

2.5 Fitting Utility Comparison

2.5.1 Common Algorithms

Fitting orbital elements, an exercise once limited to the Solar System, is now possible for thousands of stellar binaries and exoplanetary systems. This was enabled not only by the advancement of the observing techniques, but also the software tools to perform the fitting to the observed data. These technological advancements increased the number of types of observational data and their frequency, necessitating the development of more sophisticated algorithms to explore the parameter space of the full Keplerian model for two body systems. Some of these algorithms have been focused on the finding the best-fitting set of parameters, with others more suited to estimating the uncertainties in the fit or even the distribution of the solutions around it.

Nonlinear models, such as the Keplerian model, may produce likelihood functions with many local optima (but only one global optimum) [78]. For these models, there is no generalized approach to navigate the parameter space in order to find their global optimum. Instead, the collection of approaches can be separated into two categories: those that randomly search, and those that home in on the optimum from an initial guess [78]. There are many methods that implement stochastic sampling to randomly search the parameter space, including Simulated Annealing (SA). As covered earlier in Section 2.3.3, SA introduces a temperature factor to the Metropolis-Hastings algorithm to initially explore a wide range of the parameter space and slowly cools into (hopefully) the global optimum. By starting SA at a high temperature, the particular starting position has little impact on the resulting set of best-fit parameters. In the other category, one of the most commonly applied gradient decent methods to refine an initial guess is Levenberg-Marquardt (LM) [112, 130]. The LM method is a form of iterative linearization, where the χ^2 distribution about some point in the parameter space is approximated with a Taylor series expansion to efficiently descend towards the local optimum. While both the SA and LM methods are suitable for finding progressively better solutions, the reduced sensitivity to the starting position with SA makes it preferable in cases where there is no previously estimated place to initialize the search.

Table 2.3. Fitting Utility Comparison

Title If Any	Ref [a]	Fits RV	Fits Astrometry	Fits 3-D	Algorithms[b]	Open-Source	Free[c]	Code Language
RVLIN	M92	✓	✗	✗	LM	✓	✗	IDL
···	G05	✓	✗	✗	MCMC+PT	✗	✗	Mathematica
EXOFIT	B09	✓	✗	✗	MCMC	✓	✗	R, C
Systemic	M09	✓	✗	✗	LM, SA, MCMC	✓	✓	Java, R, C
EXOFAST	E13	✓	✗	✗	DE-MC	✓	✗	IDL
RUN DMC	N14	✓	✗	✗	DE-MC	✗	✓	C++
rvfit	I15	✓	✗	✗	SA, MCMC	✓	✗	IDL
OrbGrid	H89	✗	✓**	✗	grid search	✗	?*	?*
···	I08	✗	✓	✗	SA, MCMC	✗	✗	IDL
ORBIT	T92	✓	✓**	✓[d]	LM	✗	✓	Fortran
VBSB2	P98	✓	✓**	✓[d]	SA, LM	✗	✓	C
···	W09	✓	✓	✓[e]	LM	✗[f]	✗	IDL
BASE	SH12	✓	✓	✓[d]	MCMC+PT	✗	✓	GFortran
···	C12	✓	✓	✓[g]	MCMC	✗	?*	?*
ExoSOFT	here	✓	✓	✓	MC, SA, ST, MCMC	✓	✓	Python & C++

[a] Key reference(s). H89: Hartkopf et al. [83]; T92: Tokovinin [185][71, 187]; M92: Marcy & Butler [123][197]; P98: Pourbaix [158]; G05: Gregory [79]; I08: Liu et al. [115], with code written by Michael J. Ireland; B09: Balan & Lahav [11]; M09: Meschiari et al. [135]; W09: Wright & Howard [198]; SH12: Schulze-Hartung et al. [170]; C12: Crepp et al. [40]; E13: Eastman et al. [56]; N14: Nelson et al. [150]; I15: Iglesias-Marzoa et al. [95].

[b] LM: Levenberg-Marquardt; MC: simple Monte Carlo; SA: Simulated Annealing; ST: Sigma Tuning; MCMC: Markov Chain Monte Carlo; PT: Parallel Tempering, DE-MC: Differential Evolution MCMC.

[c] Free to compile and runs on all common operating systems.

[d] No direct or indirect fitting to the masses of either body involved.

[e] Indirectly calculates masses rather than allowing them to be directly varied parameters.

[f] Versions of the radial velocity fitting component RVLIN available publicly.

[g] Neither m_1 or ϖ are varied parameters.

* Unknown, as no information is available in the literature or from personal communication.

** Designed for interferometric astrometry.

Rather than separate the two goals of finding the best fitting parameters and estimating their uncertainties, a third algorithm category attempts to do perform these tasks simultaneously. Three of those listed in Table 2.3 which fall into this category are MCMC, standard Monte Carlo (MC) and 'grid search'. Through dependent sampling, MCMC directly draws parameter values from the posterior probability distributions, for further details see Section 2.3.2 of this chapter. The approach by the other two of these, instead approximate the posteriors using 'brute force'. The primary difference between them is that MC draws its samples completely randomly from the prior distributions, whereas grid search implements a pre-defined grid of the parameter space to be sequentially sampled. As discussed in Section 2.3.2, such approaches can be useful to evaluate the posteriors of models with few parameters, but can be computationally impractical for those with many. For these models with many parameters, the uncertainties can instead be estimated with MCMC or a form of 'bootstrapping'.

Assuming that the data consist of a set of independent and identically distributed data points, a re-sampling technique such as bootstrap can be applied to estimate the errors of a model's fit parameters. This approach works by drawing a new data set that is then fit with the same algorithm as for the real data set, to measure how much the best-fit changes. The new data sets are made by drawing randomly from the real data set with replacement. By repeating this process, the range of difference between the fits to the new data sets and that to the real one is used to estimate the uncertainties in the best-fit parameters for the real data. Bayesian approaches, like MCMC, provide more robust estimates of the parameter uncertainties, especially in cases where the uncertainties are large [198].

Although standard MCMC is effective at sampling the posterior probability distributions of models of many parameters, Gregory [79], Nelson et al. [150], Schulze-Hartung et al. [170] and Eastman et al. [56] implemented additional multi-processing techniques to help overcome the difficulties when fitting multi-planet Keplerian models to radial velocity data. These include Parallel-Tempering (PT) and Differential Evolution MCMC (DE-MC). PT can be considered a hybrid of SA and MCMC, with multiple Markov Chains all running at different temperatures in parallel. Periodically a swap function determines if adjacent chains should interchange their latest parameter set. The goal of this is to have the 'cold chain' sampling near the best-set of parameters found so far, and the hottest chain to broadly explore the regions with the lowest probability to ensure no small regions of global parameter space with high probability are missed. This approach is particularly useful when the posteriors contain multiple widely separated peaks, a situation in which standard MCMC typically operates poorly. Similarly, DE-MC combines the Differential Evolution genetic algorithm with MCMC to simultaneously optimize both the direction and sampling width of a Markov Chain while it is running [26, 150, 175]. The specific version implemented in RUN DMC [150], has an N-body integrator to calculate the impact of the orbital parameters found for multi-planet systems showing strong inter-planet interactions. The added computational complexity of this approach limits its full-scale use to powerful computers with discrete graphics processor units. Therefore, implementing features such as PT or those of RUN DMC add complexity to the code not necessary for the single companion systems ExoSOFT was originally designed for, and shall be considered for future versions of ExoSOFT.

Table 2.4. Fitting Algorithm Pro/Con Comparison

Algorithm	Pro/Con
Pros:	
LM	Fast, when provided a good starting position in a smooth likelihood distribution
SA	Less sensitive to starting position or likelihood distribution shape
MC/grid search	Simple way to approximate the posteriors of models with few parameters
bootstrap	Quick way to estimate the errors of simple models
MCMC	Robust error estimation for parameters of two-body Keplerian models
PT/DE-MC	Highly adaptive and intelligent way to navigate complicated multi-planet cases
Cons:	
LM	Operates poorly with bad starting positions or in 'bumpy' likelihood territory
SA	Does not always find the global optimum in highly modal likelihood spaces
MC/grid search	Typically too slow for models with more than a few parameters
bootstrap	Commonly insufficient for the parameters of Keplerian models
MCMC	Sometimes slow, or insufficient, for complicated multi-planet cases
PT/DE-MC	Unnecessarily complicated for most two-body cases

2.5.2 Available Software

A collection of the software tools developed to solve for the orbital elements of binary stars and exoplanetary systems is listed in Table 2.3; the algorithms' strengths and weaknesses are summarized in Table 2.4. Those designed specifically to fit radial velocity measurements alone include RVLIN [123, 197], Systemic [135], RUN DMC [150], rvfit [95], EXOFAST [56], EXOFIT [11], and that of Gregory [79]. OrbGrid [83] and that written by Michael J. Ireland and discussed in Liu et al. [115], fit astrometry alone, from interferometric observations taken with the CHARA array and direct imaging, respectively. Five tools in Table 2.3 were developed to perform 3-D fitting, those being ORBIT [185], VBSB2 [158], BASE [170], that discussed in Crepp et al. [40], and a package which adds the capability to fit astrometric data to RVLIN, presented in Wright & Howard [198]. Each of these software tools utilizes one or more parameter space exploration algorithms, observational data types, and programming languages. In spite of all having their own specific set of features, they also have important shortcomings or limitations that motivated me to develop ExoSOFT.

2.5.3 ExoSOFT Robustness and Efficiency

I sought a combination of the algorithms in Table 2.4 to ensure ExoSOFT's robustness for a wide range of systems. While popular, the LM method suffers from the need for starting position in the vicinity of the global optimum, and the fact that by not being stochastic, it has a tendency to repeatedly attempt a steepest decent into shallow valleys of the objective function with degenerate parameters [159]. To overcome these difficulties, I have chosen to instead use a version of the SA method for this important stage of ExoSOFT. The temperature factor and stochastic sampling allows it to start from positions

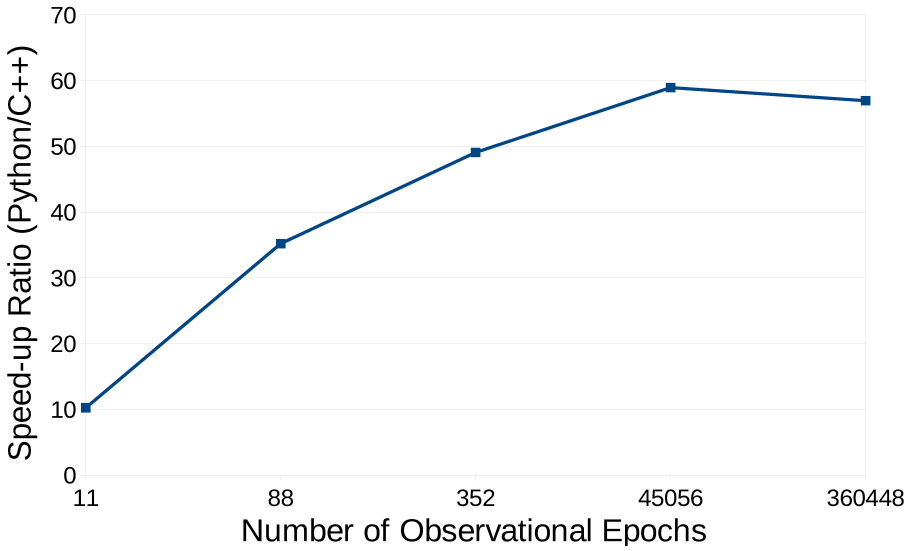

Figure 2.5 Speed-up of the Keplerian model used in ExoSOFT written in C++, interfaced using SWIG, over that written in pure Python. The C++ version is between 10-58 times faster, depending on the number of observational epochs.

with low likelihood, and 'smooths' over topographical bumps in the likelihood distributions caused by local optima. With no provided starting position, the specific implementation in ExoSOFT first randomly draws parameters from the global parameter space with simple MC until a set of parameters satisfying $\chi^2_\nu \lesssim 250$ is found to start SA with. Additionally, both the repeated heating and cooling, and maintaining a list of the best fits achieved so far, make sure the process used in ExoSOFT is sufficiently robust to find suitable starting positions for the later MCMC chains for any system being investigated.

In order to ensure the efficiency of MCMC sampling, the width for each parameter's proposal distribution must be optimized. As discussed in Section 2.3.3 this is accomplished with Sigma Tuning (ST). Similar to the automation implemented into the SA algorithm used in ExoSOFT, the ST algorithm was also automated. The periodic calculation of the acceptance rates and subsequent tuning of the proposal widths is only continued until they all achieve a ∼25–35% acceptance 10 times in a row. This ensures that the algorithm only operates for the minimum number of samples to achieve stable, optimized proposal widths. Both components of the MCMC initialization stages, finding a starting position and optimizing the proposal widths, are automated and efficient.

The algorithms available in ExoSOFT (MC, SA, ST, MCMC) all utilize the same code for the Keplerian model, written in C++ and interfaced with the Python code using SWIG. Testing of identical versions of the model written in C++ and pure Python showed a trend of increasing speed advantage with number of observational epochs until this leveled out to C++ being ∼ 55–60 times faster than pure Python, see Figure 2.5. With this, I suggest a multi-stage approach of automated SA-ST for initialization and long MCMC to explore the posterior probability distributions. This approach was tested using a wide range of synthetic data from Earth analogues to binary star systems, and

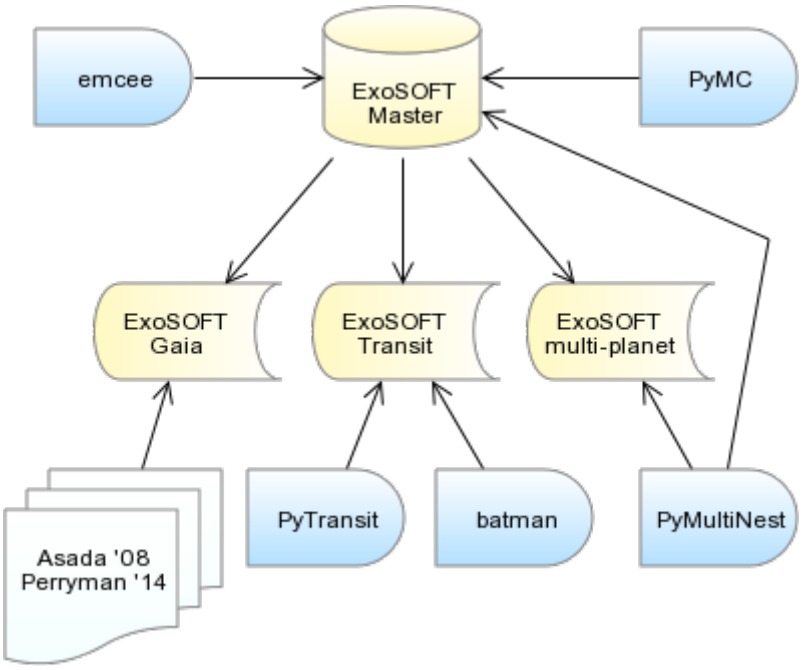

Figure 2.6 Basic flowchart of the possible future branches of ExoSOFT on GitHub and the integration of other Python packages on GitHub. The 'Master' and future branches are shown in yellow, the other related GitHub repositories that could be integrated in blue, and the papers from which to draw equational forms to create a model for fitting *Gaia*-type astrometry data in white [7, 154].

in real-world applications to V450 And in Chapter 3, and the four planets of the HR 8799 system in Chapter 4. These all verify ExoSOFT's capability to fit the observed data of any two-body system without prior knowledge of the regions of high likelihood, and only simple and wide, physically justified restrictions to the global parameter space.

2.5.4 ExoSOFT Uniqueness

Software development practices have advanced alongside improving algorithms and languages. The common standard today involves developing the code in an on-line repository, with version control and access from anywhere; the most widely used on-line repository system is GitHub[6]. Developing ExoSOFT on GitHub allows for easy access and international collaboration that can lead to additional functionalities, including other parameter space exploration algorithms and the capability to fit to other forms of observational data. Some of the algorithms that could be integrated into ExoSOFT are available in Python packages also hosted on GitHub, including PyMC[7] [66], emcee[8] [70] and PyMultiNest[9] [63]. The equational forms of the specific Keplerian models to fit to astrometry from *Gaia*, or transit photometry data, have been well documented in papers such as Asada [7], Casertano et al. [30], Mandel & Agol [122], Perryman et al. [154]; the transit model of Mandel & Agol [122] has

[6] www.github.com
[7] https://github.com/pymc-devs/pymc
[8] https://github.com/dfm/emcee
[9] https://github.com/JohannesBuchner/PyMultiNest

been implemented in Python packages on GitHub, including PyTransit[10] [151] and batman[11] [107]. From these, different flavors of ExoSOFT could be developed as individual branches from the main repository, or added to the main model to allow it to fit a wider array of data types itself. A graphical representation of the possible future structure of ExoSOFT's GitHub repository is given in Figure 2.6. While ExoSOFT was initially motivated by the need to fit to radial velocity and astrometry from direct imaging, its open-source development on GitHub enables it to take on additional capabilities including new algorithms to explore parameter space, fit multi-planet systems, and accept any form of observational data.

ExoSOFT offers a unique collection of functionalities that are not simultaneously available from any other tool. It is the only tool that:

1. is open-source and fits radial velocity and astrometry simultaneously;
2. performs initialization, optimization and MCMC sequentially and in a largely automated fashion;
3. comes packaged with a suite of automated post-processing utilities to analyze and summarize the results;
4. has been written largely in the popular Python programming language; and
5. performs the above and is hosted on GitHub, allowing for easy integration with other Python packages already on GitHub (PyMC, emcee, PyMultiNest, PyTransit, batman).

The popularity and broad use of Python, combined with an open-source development platform on GitHub, will maximize the opportunities for ExoSOFT's expansion to include additional parameter space exploration algorithms and the ability to fit further forms of observational data. All of these future advancements to ExoSOFT will be hosted publicly for the use by the entire astronomical community, available for any stellar binary or exoplanet investigations.

2.6 ExoSOFT in Use

ExoSOFT was designed with ease of use in mind. The settings available to the user have been collected into a single settings.py file; ExoSOFT may then be run with a single command. When using ExoSOFT for a new astronomical system for the first time, the user would need to fill in any radial velocity and astrometric data into their respective files and update a few parameters in the settings file. The default values within this settings file are valid for a wide range of astronomical systems, minimizing the number of those that need to be adjusted to the ranges of allowed parameter values, the choice of priors for each parameter and the number of CPUs to be utilized. Table 2.5 lists the only parameters most users will need do adjust to fit a new system. At this early stage, the user

[10] https://github.com/hpparvi/PyTransit
[11] https://github.com/lkreidberg/batman

Table 2.5. Most Commonly Adjusted Settings in ExoSOFT's Settings File

Setting	Explanation	Typical Values/Ranges
m_1 Min/Max	Minimum and maximum range for m_1	[0.01 $M_\odot$, 5 $M_\odot$]
m_2 Min/Max	Minimum and maximum range for m_2	[0.01 M_J, 2 $M_\odot$]
ϖ	Previously measured parallax	[1 mas, 100 mas]
σ_ϖ	Uncertainty in measured parallax	[1 mas, 5 mas]
m_1 prior	Prior for m_1	PDMF or IMF *
m_2 prior	Prior for m_2	PDMF, IMF or CMF *
# chains	Number of chains to run	[2, # CPUs]
start Params	Parameter values to start from	depends on system
stages	Stages to run	SA, SA-ST, SA-ST-MCMC, MC, MCMC

* Optional priors for the masses discussed in Section 2.3.2 from Chabrier [31], Metchev & Hillenbrand [136].

may want to increase the number of messages being printed to the console with the 'logLevel' setting, to monitor ExoSOFT's progress. Should they wish to make changes, they simply need to update the associated settings in the settings file and re-run the command line call to ExoSOFT. This process of using the software is graphically represented as a flowchart in Figure 2.7.

Outside of the settings built into ExoSOFT, the user also has the option to add their own priors for each of the model parameters. This can easily be done by adding a new Python function to the priors.py file, using the same input/output format as the priors already available. While the results from recent survey papers [93, 101, 102, 171] will be taken into account as additional choices for the eccentricity prior, some users might wish to write their own to test the impact of a specific prior distribution. There are also a number of advanced settings more experienced users could tune to make ExoSOFT more effective for their specific system of investigation. For example, the default settings for the SA stage will perform multiple $1{\times}10^5$ sample iterations, initially starting from a temperature of 50. When running ExoSOFT on only 1-2 CPUs, it could be more effective to run longer iterations, starting from a higher temperature, by adjusting the 'nSAsamp' and 'strtTemp' settings. Another case where a user would want to change the defaults is when running very long ($> 1 \times 10^7$) MCMC chains with strongly correlated parameters. For such long runs, the output data file sizes can be reduced by decreasing the rate samples are stored to disk with the 'saveInt' setting. Following the completion of an ExoSOFT run after adjusting these more advanced settings, it is important to review the changes they made in the results summarized in the RESULTS.txt file to ensure they achieved the desired effect.

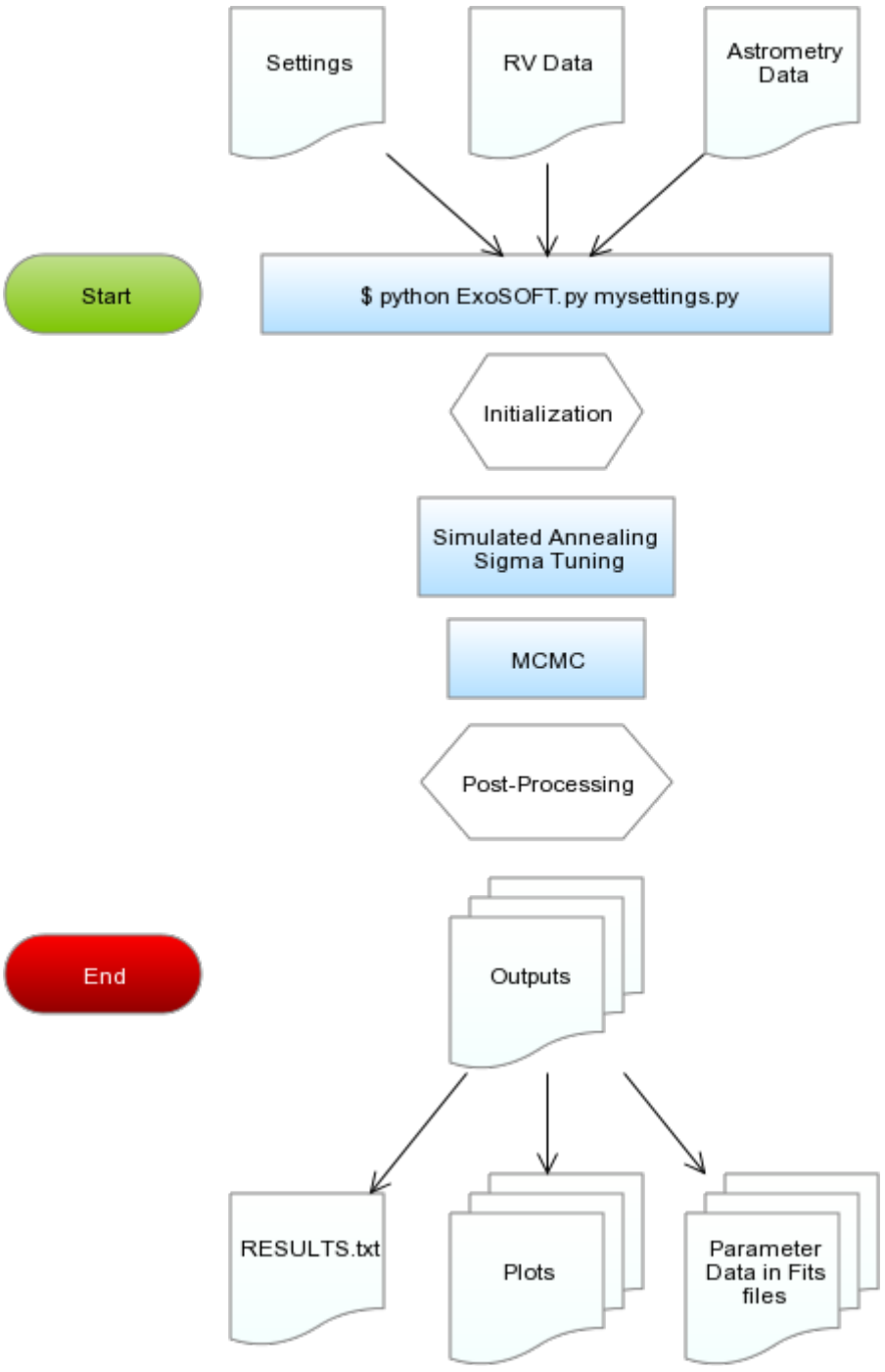

Figure 2.7 Basic flowchart of ExoSOFT in use. Measured radial velocity and astrometry data are used along with the settings file as the inputs, and ExoSOFT is started with a simple command call. Produced during post-processing, the primary outputs include a summary of the important analysis statistics and results in RESULTS.txt, along with the graphical plots of the orbits, the posterior probability distributions and the parameter data files. See Figures 2.2, 2.3 and 2.4 for examples of the figures ExoSOFT can produce.

With only a few simple changes required to the default settings and single command to start it, ExoSOFT comes ready for use by anyone who wishes to try it. For users with some background understanding of the algorithms involved, there are advanced settings available to be adjusted should they wish to try to make it outperform its defaults. Together, these settings and ExoSOFT's overall capabilities make it a useful orbit fitting software tool for stellar binary and exoplanet investigations.

2.7 Summary and Future Prospects of ExoSOFT

I have presented ExoSOFT, a toolbox for the Keplerian orbital analysis of exoplanets and binary star systems. It is free to compile, open source, fits any combination of astrometric and radial velocity data, and offers four parameter space exploration techniques, including MCMC. The suggested first two stages of Simulated Annealing and Sigma Tuning perform the initialization and optimizations necessary for MCMC to operate efficiently. Following this, trial runs can be used to determine how many samples to draw to ensure the chains sufficiently converge to the posterior probability distributions. ExoSOFT is packaged together with a set of post-processing and plotting routines to summarize the results. Verifications were performed by fitting noisy synthetic data produced with an independent Keplerian model for a variety of systems ranging the entire parameter space. Examples of its use on real data include that for the V450 And system in Chapter 3, the multi-system HR 8799 in Chapter 4, and the τ Boo AB binary in Mede & Brandt [134].

Simultaneous fitting to both radial velocity and astrometric data helps to break the degeneracies in Keplerian model parameters. The dynamical mass estimates of the companion and the well-constrained values of the other orbital elements found in this way are important clues to sub-stellar formation and evolution. The companion's mass and age may be used to place constraints on the input parameters of atmospheric models for brown dwarf and low mass stars. The initial conditions of sub-stellar objects remain uncertain, with theoretical predictions ranging from hot-start to cold-start scenarios [125]. Mass, eccentricity and separation are also important to help distinguish between the variety of dynamical evolution possibilities in multi-planet systems.

Recent surveys aiming at the high-end range of sub-stellar mass companions [193] and at the lower end [88] show how the capabilities of new instruments are expanding the range of companions detectable with the radial velocity method. Complementary to these, observations of HR 8799 with SPHERE and GPI [eg. 4, 22, 96, 200] highlight the improved astrometric and characterization capaiblities with next generation integral field spectrographs. Combining ground based facilities with the *Gaia* spacecraft will broaden not only the mass range, but also the number of objects simultaneously observed with both radial velocity and direct imaging techniques. With its capacity to simultaneously fit both of these data types, effectively explore the parameter space, and with its post-processing and plotting tools, ExoSOFT is well-suited to constrain the orbits of newly discovered systems.

Chapter 3

Application of ExoSOFT to V450 Andromedae

In this chapter we report the first direct imaging detection of a low-mass companion to the star V450 Andromeda. With the new addition of astrometry derived from the direct imaging data in combination with the long baseline of radial velocity measurements from three different instruments, I performed joint analysis orbital fitting to provide the first estimates of the companion's dynamical mass. Thanks to this more encompassing collection of data and a new orbit fitting toolbox, I successfully showed the companion to be a low-mass star ($m_2 = 0.282^{+0.042}_{-0.023}$ M$\odot$), >5 times greater than its previously estimated value based purely on short baseline radial velocity data. This work demonstrates that combinations of RV and direct imaging data can improve the characterization of low-mass stars, brown dwarfs, and eventually exoplanets.

This chapter is based on the paper:

Title: "SEEDS direct imaging of the RV-detected companion to V450 Andromedae, and characterization of the system."

First Author: K. G. Hełminiak

Status: At the time of this thesis' submission, the paper is under review for acceptance to The Astrophysical Journal, with the application number #ApJ102021.

Cite: Hełminiak et al. [90]

Authorization to use the material from said paper has been included along with the submission of this thesis in accordance with the research ethics policies of The University of Tokyo.

3.1 Motivation to Study the V450 And System

The radial velocity (RV) technique has been one of the most effective to survey exoplanets and brown dwarfs since 1980s, the decade in which regular RV surveys began [65]. However, the time baselines of these initial RV observations were so short that detecting long-period planets was relatively impractical. On the other hand, the direct imaging technique has been successful in exoplanet detection for over a decade now [36], but is still limited to objects relatively distant from the parent star, even despite a tremendous improvement in recent years that allowed us to discover less massive planets on closer orbits [47, 110, 128, 162]. Only very recently, thanks to the long-time coverage of RV data, and development of new generation instruments for both RV measurements and high contrast imaging at narrow separations, have the discovery spaces started to overlap, allowing for some objects to be detectable by both techniques. This opens new possibilities in characterization of extrasolar planets, brown dwarfs and low-mass stars. Only a few examples of RV and imaging detections of a companion have been known to date, [i.e. 39, 41, 42, 43, 44, 166] but their characterisations are either inadequate or uncertain due to incomplete data coverage of the orbit, or because the uncertainties in distance and mass of the primary were not adequately included in the final error budget. A notable case is, however, HD 16760b, where initial fitting to RV data indicated a minimum mass at the border between the planetary and brown dwarf regimes ($\sim$13 M_J) [25, 169]. Although no simultaneous fit to RV and astrometric data was performed, direct imaging reported in Evans et al. [61] revealed a low-inclination orbit, and the mass of the companion of 0.28(4) $M_\odot$. This case demonstrates how inaccurate the RV-based lower limit can be, and how important is to supplement RV detections with astrometric data [see also 193].

Here we present an example where RV measurements span almost a whole orbital period, which allows us to obtain secure dynamical masses of both stars. For the first time, the orbital fit is obtained from all data simultaneously, and masses of both components are directly calculated. Basic information about the target is given in Section 3.2. Section 3.3 describes the observational data used in this work. The orbital analysis is described in Section 3.4, and I summarise our work in Section 3.5.

3.2 The Target

V450 And is a magnetically active G-type star located about 27 pc from the Sun. The low-mass companion on a long-period orbit was first announced by Perrier et al. [153, hereafter P03], and a preliminary fit was performed on 19 ELODIE measurements spanning from January 1998 to December 2002. P03 obtained an orbital period of $\simeq$3000 days, a small eccentricity of 0.14, a companion minimum mass of 52 M_J, and a projected separation of 4.3 AU, or 164 mas at the distance to the system, assuming the mass of the host to be 1.09 $M_\odot$. They had, however, poor coverage of the true orbital period, leading to them underestimating it, as well as the minimum mass. They also searched for the companion with adaptive optics imaging, but failed to identify it in their data. More such

Table 3.1. Observing Log

Obs. Date (UT)	$N_{\rm exp}$	$t_{\rm tot}$ (s)	Filter	Mean Airmass	mag
2012 Nov 05	25	125	H	1.13	4.10 ± 0.05
–	10	50	$K_{\rm s}$	1.09	3.85 ± 0.07
2013 Jan 02	16	40	J	1.39	4.18 ± 0.08
–	7	62	H	1.43	4.07 ± 0.06
–	16	24	$K_{\rm s}$	1.42	3.82 ± 0.08
2013 Oct 16	13	195	H	2.19	4.05 ± 0.04
2015 Jan 08	50	575	H	1.08	4.03 ± 0.03

attempts were made later, but also without success [137, 164, 186]. We present the first positive detection of V450 And B with high-contrast imaging.

Further detail regarding the target can be found in section 2 of the original paper [90].

3.3 Observations and Data

3.3.1 SEEDS Observations

We observed V450 And as part of the Strategic Exploration of Exoplanets and Disks with Subaru [SEEDS; 180] survey, which has searched for exoplanets and imaged circumstellar disks around hundreds of nearby stars [e.g., 84, 97, 183]. We observed V450 And with the HiCIAO camera [178], a high-contrast imaging instrument on the Subaru Telescope. The adaptive optics system AO188 [86] was used to correct the point spread function (PSF) degradation caused by the Earth's atmospheric turbulence. AO188's atmospheric dispersion corrector [58] removed the chromaticity of atmospheric refraction.

Table 3.1 shows the observing log for V450 And observations. We observed the star in angular differential imaging (ADI) mode [126] to distinguish companion candidates from diffraction speckles, and also allowed the central star's PSF to saturate in order to search for faint companions. The only companion candidate was about 40 times fainter than V450 And in the H-band; follow-up observations confirmed it as a low-mass stellar companion. Figure 3.1 shows the primary together with its companion, V450 And B, using a logarithmic stretch. Because of the modest contrast between the primary and secondary, we used unsaturated images in each observing sequence to measure the astrometry of the system and to track its orbital motion.

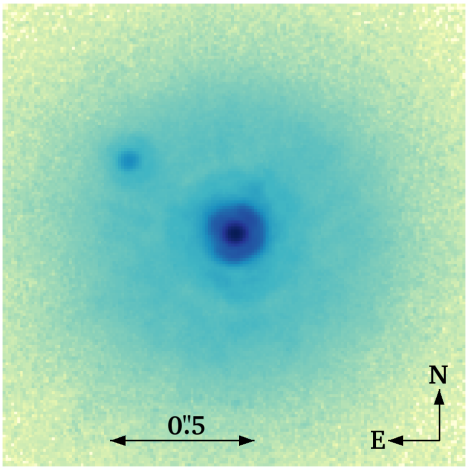

Figure 3.1 H-band image of V450And showing its M dwarf companion about 0.″44 to the northeast. The stretch is logarithmic; the companion is about 40 times fainter in the H-band than the G5 primary.

Table 3.2. Astrometric Measurements

Obs. Date (UT)	MJD (days)	Separation Angle (mas)	Position Angle (°)
2012 Nov 05	56236.342	437.87 ± 0.38	73.095 ± 0.061
2013 Jan 02	56294.375	437.5 ± 1.2	71.76 ± 0.17
2013 Oct 16	56581.652	432.7[a]± 1.2	65.512[a]± 0.089
2015 Jan 08	57030.244	422.63 ± 0.86	55.52 ± 0.14

[a] Corrected for the effect of atmospheric refraction. The separation and position angle before the correction are 432.3 mas and 65.°520, respectively.

The distortion was measured by observing a globular cluster and correcting stellar positions to their calibrated positions in *Hubble Space Telescope* data. We used the ACORNS pipeline [27] to correct bad pixels, remove correlated read noise, and to correct the field distortion. No high-contrast PSF subtraction algorithms were applied, instead we directly fit for the PSF centroids in the unsaturated data using elliptical Gaussians. By fitting the PSF cores in the unsaturated data, we achieve much higher astrometric precision than is typically of high-contrast imaging. Our resulting astrometry are listed in Table 3.2, and an example of a final image prior to the subtraction of the primary star's radial profile is shown for the 2015-01-08 observations in Figure 3.1. See Hełminiak et al. [90] for details.

3.3.2 Archival Spectra and Radial Velocities

The complete set of archival spectra and RV measurements consists of 80 observations coming from three instruments on two telescopes. The observations cover a total temporal baseline of 18 years, nearly a full orbital period. Of the 80 epochs of data extracted from their archives, 25 RV measurements were taken with the recently decommissioned ELODIE spectrograph for the 1.9-m telescope at the Observatoire de Haute-Provence (OHP) [145], including six previously unpublished by P03, with a total time span of 2536 days (1998 January 8 to 2004 December 18). Another 25 spectra were taken with ELODIE's replacement SOPHIE between 2013 September 26 and 2016 February 29 (time span: 886 days). Lastly, an additional 30 data points made with the Hamilton spectrograph on the 3.5-m Shane telescope at the Lick observatory, spanning 5012 days (1998 January 18 to 2011 October 9), which is the longest time span of all the data sets we used. The Hamilton data also cover the gap between ELODIE and SOPHIE observations, which was crucial for merging all the data in the orbital fit.

Further detail regarding the archival RV data can be found in section 3.3 of the original paper [90].

3.4 Orbital Solution

Both the radial velocity and astrometric data were fit simultaneously with a Keplerian model to solve for the system's orbital parameters. The full solution includes 9 parameters, with a further 3 for the spectrograph offsets. To perform the fitting, I adopt a Bayesian approach similar to that discussed in Ford [68]. The posterior probability distributions for the model parameters are proportional to the product of the model parameter's likelihood, $\mathscr{L}(\text{Model})$, and their prior probability based on previous knowledge, $p(\text{Model})$. Assuming the data errors (σ) are independent and follow a Gaussian distribution, the likelihood may be written as

$$\mathscr{L}(\text{Model}) = \exp\left(-\frac{\chi^2}{2}\right) \tag{3.1}$$

with

$$\chi^2 = \sum_i \frac{(\text{Model}_i - \text{Data}_i)^2}{\sigma_i^2}, \tag{3.2}$$

and the priors used in my model fitting are summarized in Table 3.3.

The Keplerian model includes the directly varied parameters: m_1, m_2, e, P, ϖ, T_0, i, Ω, ω, γ_1, γ_2, γ_3; respectively these are, the mass of the primary star, mass of companion, eccentricity, period, parallax, time of last periapsis, inclination, longitude of the ascending node, argument of periapsis, and the radial velocity offsets for each spectrograph (ELODIE, Hamilton and SOPHIE). Fitting these 12 parameters with a direct sampling approach, such as simple Monte Carlo, can be difficult due to their possibly complicated likelihood topography. To overcome this I use the Markov Chain Monte Carlo

Table 3.3. Adopted Bayesian priors

Parameter	Prior
ϖ	Gaussian[a] $\times (1/\varpi^4)$
e	$p(e) \propto e^b$
P	Logarithmic
i	$p(i) \propto \sin(i)$
m_1 & m_2	PDMF[c]
others	Uniform

[a] *Hipparcos* value of 37.25 ± 0.55 mas, from [190]

[b] From Duquennoy & Mayor [55]

[c] Present-Day Mass Function [32, Table 1]

(MCMC) features of a new software package entitled the Exoplanet Simple Orbit Fitting Toolbox (ExoSOFT; K. Mede & T. Brandt 2016, submitted). This toolbox explores the parameter space using a multi-stage approach ending in MCMC. It is capable of fitting any combination of astrometry and radial velocity data, and performs automated post-processing to summarize the results. The code was written primarily in the Python programming language with the computationally intensive model in C++.

The first orbital fitting to the V450 And system was discussed in P03, which utilized an updated version of the ORBIT tool [185], described in Forveille et al. [71]. The tool performs a gradient decent through the parameter space with a Levenberg-Marquardt minimization technique. Fitting to the radial velocity data available at the time, spanning ∼4.5 years, and assuming a fixed mass of 1.09 $M_\odot$ for the primary star, the team reported a preliminary orbital solution. The best-fit values from P03 were: P≈3000days, $e = 0.14$, $K_1 = 0.694 kms^{-1}$, $m_2 \sin(i) = 52 M_J$, and $a = 4.3 AU$. For comparison I conducted fitting to the same data using ExoSOFT and summarize the results in Table 3.4. My best-fit has an orbital period of ∼11 years, 3 years longer than that of P03, thereby increasing the estimated companion mass to $m_2 \sin(i) = 59 M_J$. I performed the fitting with the RV instrumental offset (γ_{ELO}) as a free parameter first and again with it fixed. Both produced nearly identical best fit values, although the posterior probability distributions and relative 1σ confidence regions were significantly broader when it was a free parameter. The values given in Table 3.4 were found using the best-fit value for γ_{ELO} (5876 $m\,s^{-1}$) as a fixed parameter. Discrepancies between the ExoSOFT and P03 results could be explained by a difference in the γ_{ELO} values, although P03 did not report a value to confirm this hypothesis.

Table 3.4. ExoSOFT Fit to P03 RV Data for Comparison

Parameter	Best-fit	Median	ϵ^{a}	P03 Best-fit
e ( )	0.108	0.119	0.026	0.14
T_0 (JD-2452270)	86	20	260	···
P (yr)	11.2	11.5	1.3	8.2
ω_2 (°)	348	341	29	···
a_{total} (AU)	5.18	5.26	0.39	4.3
K ($\mathrm{m\,s^{-1}}$)	713.0	713.1	7.8	694
$m_2 \sin(i)(M_J)$	59.1	59.5	3.1	52
χ^2 $(\nu)^{c}$	7.47 (14)	···	···	···

[a] Approximate 1σ uncertainty: 68.3% of the posterior probability lies within ϵ of the median

[c] ν represents the number of degrees of freedom (dof) during MCMC fitting ν=(19 RV epochs)(1 dimension)-5 varied params=14 dof

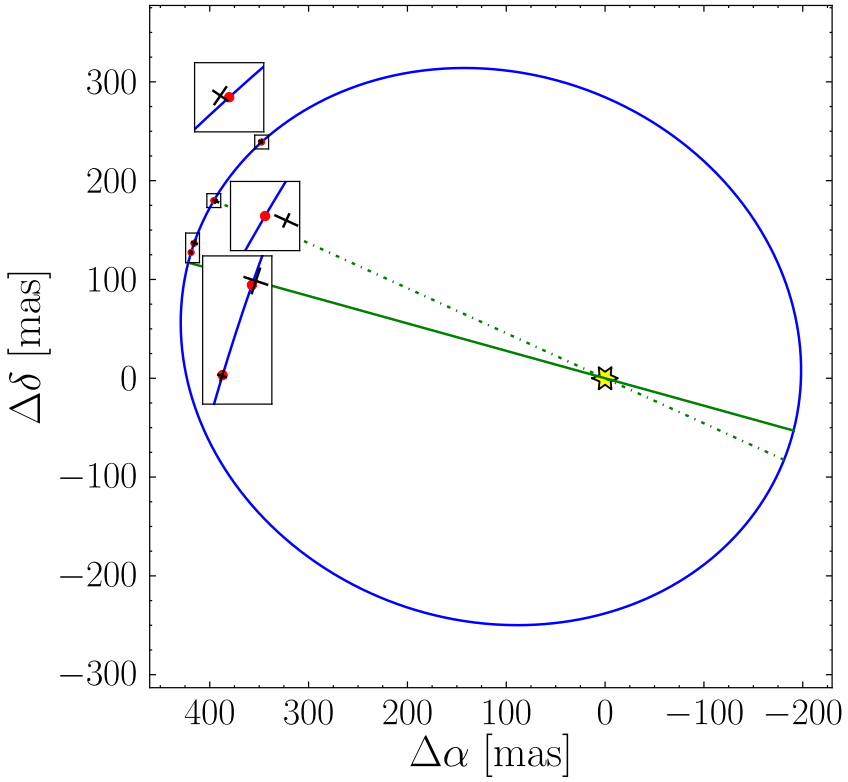

Figure 3.2 Astrometric orbit of V450 And B relative to A (marked as yellow star). The line of apsides and line of nodes are marked with the solid and dotted green lines, respectively. Our HiCIAO measurements are shown as black crosses to indicate the astrometric errors atop the model predicted locations marked as red dots; the insets are magnified by a factor of ten.

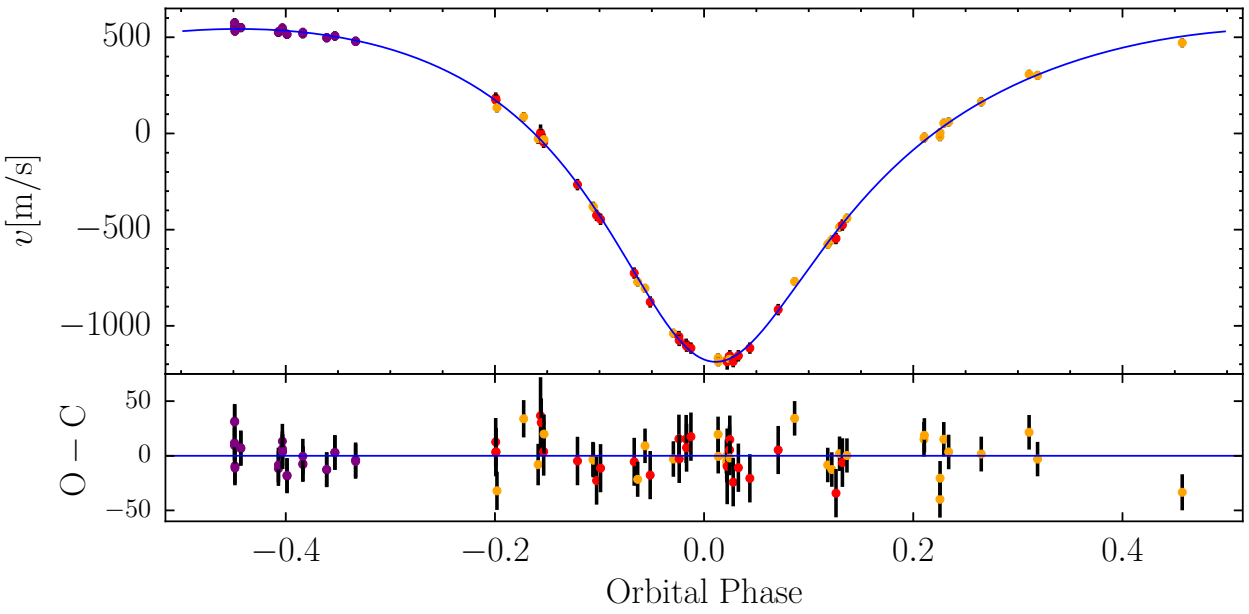

Figure 3.3 Radial velocity measurements from ELODIE (red), Hamilton (orange) and SOPHIE (purple) observations, and the fitted RV curve of V450 And A, phase-folded with the orbital period. Measurements are shifted by the offset values given in Table 3.5. The lower panel shows the residuals of the fit. The error bars include the jitter; they are also shown in the upper panel, but are comparable to the size of the points.

Prior to utilizing both forms of observational data, fits were performed with only the radial velocity data from all 3 instruments. During this, an instrument-independent jitter was added in quadrature with the estimated RV uncertainties, and adjusted until a value of 13.6 $\mathrm{m\,s^{-1}}$produced a best reduced $\chi^2 = 1$. Following this step, a full joint analysis was performed to find the posterior probability distributions of the orbital parameters. Figures 3.2 and 3.3 show the best fit orbit in both astrometry and RV. Table 3.5 summarizes both the best-fitting and median values, as they differ due to asymmetries in the posterior distributions. For the MCMC stage I ran 7 parallel chains of $1{\times}10^8$ samples each to achieve sufficient convergence to the posteriors, shown in Figure 3.4, measured by a Gelman-Rubin statistic value of 1.002. Comparing the results in Table 3.4 and Table 3.5 we can see that the additional RV data and astrometry reduced the error margins by at least an order of magnitude for all the matching parameters. This validates not only the need to use the entire ensemble of available data, but also the benefits of joint analysis.

I found that the secondary is a $0.282^{+0.042}_{-0.023}$ M$\odot$ star (suggesting it is an M dwarf) on a nearly face-on, eccentric orbit. The orbital period of 21 years is over two times longer than suggested in P03, mainly due to the much shorter time span of their data (∼4.5 years), which led to a poor determination of orbital parameters. The resulting $m_2 \sin(i)$ is therefore much larger than in P03, and the companion cannot be a brown dwarf. We were a bit fortunate that our imaging covered the apocenter passage, as this portion of the orbit displays the greatest curvature in the measured astrometry. The orbital parameters are given with a very good precision (e.g.: 0.53% in K), mainly thanks to the almost

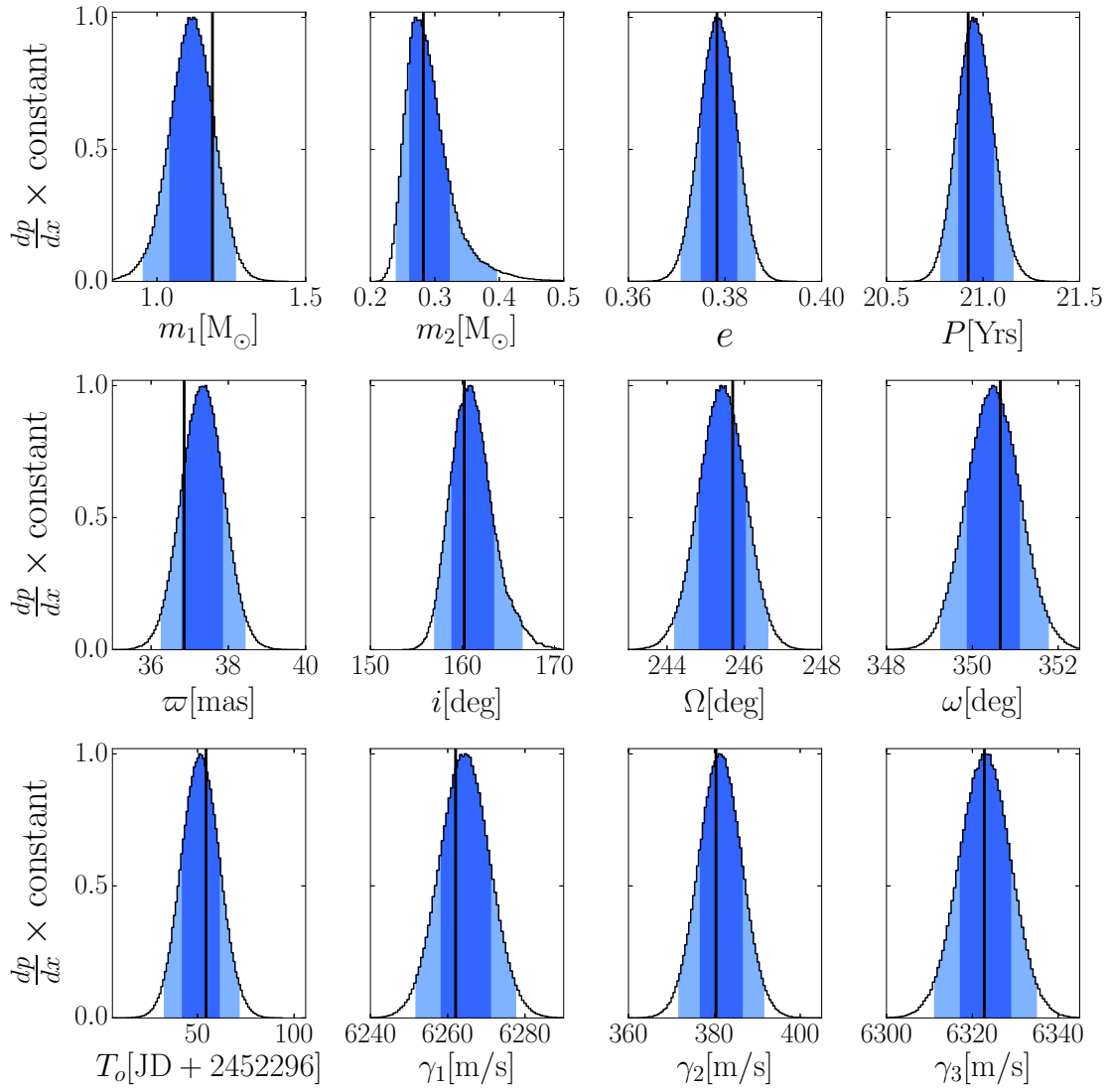

Figure 3.4 The MCMC posterior distributions of the varying parameters. Best-fit values are marked with blue vertical lines, while the dark and light blue ranges represent the 68.3 and 95.4% (1 and 2σ) confidence levels, respectively. The consecutive offsets (γ) are for the ELODIE, Hamilton, and SOPHIE instruments.

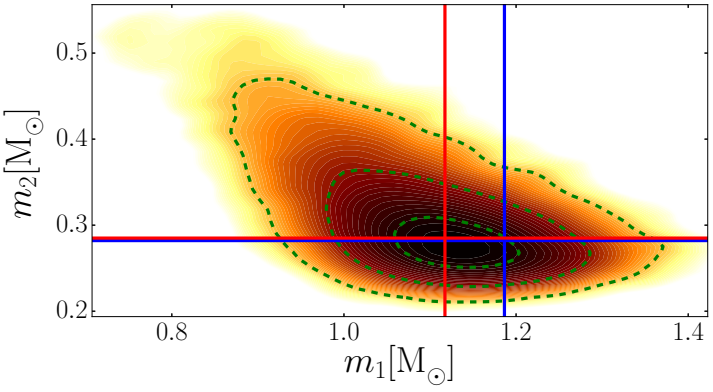

Figure 3.5 A 2-dimensional density plot for comparison of the final posterior density function for m_1 and m_2. Dashed contours indicate the 3σ, 2σ, and 1σ confidence levels, with the best fit and median values as solid blue and red lines, respectively.

Table 3.5. Results of the joint astrometric+RV Keplerian orbital fit.

Parameter	Best-fit	Median	68% range[a]
m_1 ($M_\odot$)	1.186	1.117	(1.042:1.191)
m_2 ($M_\odot$)	0.282	0.285	(0.259:0.324)
ϖ (mas)	36.86	37.34	(36.79:37.88)
e ( )	0.3783	0.3786	(0.3748:0.3824)
T_0 (JD−2452296)	54.4	51.6	(41.9:61.4)
P (yr)	20.923	20.959	(20.868:21.054)
i (°)	160.2	160.9	(158.8:163.4)
Ω_2 (°)	245.70	245.42	(244.82:246.02)
ω_2 (°)	350.65	350.49	(349.88:351.11)
$a_{\rm total}$ (AU)	8.63	8.52	(8.39:8.65)
K ($m\,s^{-1}$)	863.6	864.4	(859.8:869.0)
$\gamma_{\rm ELO}$ ($m\,s^{-1}$)[b]	6262.0	6264.4	(6257:6270)
$\gamma_{\rm Ham}$ ($m\,s^{-1}$)[b]	380.4	381.4	(376.4:386.4)
$\gamma_{\rm SOP}$ ($m\,s^{-1}$)[b]	6322.8	6323.0	(6317.0:6328.9)
χ^2 (ν)[c]	83.69 (76)	···	···

[a] Approximate 1σ uncertainty: 68.3% of the posterior probability lies in this range

[b] Radial velocity offsets: systemic velocities for ELODIE and SOPHIE, difference between the average and systemic velocity for Hamilton

[c] ν represents the number of degrees of freedom during MCMC joint fitting ν=(4 DI epochs)(2 dimensions)+(80 RV epochs)(1 dimension)−(12 varied params)=88 − 12=76 dof

complete (87%) coverage of the orbit with RV data, despite the stellar activity. The near face-on orientation of the orbit adds to the difficulty in determining the companion mass, therefore my $0.285^{+0.039}_{-0.026}$ $M_\odot$ median fit for m_2 has ∼10% error. These values arise from the choice to make both the primary star's mass and the parallax directly varied parameters, ensuring their errors are appropriately handled at every step in the MCMC chains and the resulting posterior distributions.

As shown in Figure 3.5, the posterior probability distributions for the masses m_1 and m_2 are anti-correlated. This is largely due to Kepler's third law:

$$a_{\rm total} = \left[\frac{P^2 G(m_{\rm total})}{4\pi^2}\right]^{1/3} \tag{3.3}$$

As listed in Table 3.5, both the $a_{\rm total}$ and P fits are at least ∼4 times tighter than for the masses. Equation (3.3) requires that the total mass ($m_{\rm total} = m_1 + m_2$) must also have a relatively narrow distribution, even after taking the cube of $a_{\rm total}$.

3.5 Summary and Future Prospects of Joint Orbit Fitting

In this work I have presented our analysis of a low-mass companion originally discovered with the RV technique, and since detected with high-contrast imaging. In comparison with previous work by P03, I employed in my analysis additional astrometry and more RV data, covering almost the whole orbital period. This enabled me to better constrain the orbit, as well as other crucial systems parameters. I derived the full set of orbital parameters and masses for both components, showing that the secondary is an M-type star, not a brown dwarf as suggested by P03. The combined RV and imaging data allowed me to draw a full image of the V450 And system.

The presented work may be a test case for future studies, aimed for characterisation of known brown dwarf and exoplanet candidates. Cases like V450 And, HD 16760, or objects from the recent study by Wilson et al. [193], clearly show the need to support RVs with other forms of observational data. With the capabilities of already existing extreme adaptive optics systems, like SCExAO at Subaru [98, 131], GPI at Gemini [117] or SPHERE at VLT [19], and their future generations that will be working with the upcoming 30-m class telescopes, it will be possible to detect and directly characterise companions of lower masses and shorter orbital periods than V450 And B. This may bring a revision of our knowledge of long-period brown dwarf and massive planet candidates, their distribution, initial mass function, and mechanisms of their formation, for example by pointing out objects in the "brown dwarf desert" [80, 124, 193]. Considering this upcoming wealth of astrometric and RV data for such sub-stellar companions, ExoSOFT is well situated to perform the required fitting of their orbital parameters, thereby supporting the investigations into these interesting scientific questions.

Chapter 4

Application of ExoSOFT to HR 8799

In this chapter I discuss the orbital fitting to the planets of the HR 8799 system with ExoSOFT.

The wide separation multi-planet system orbiting HR 8799 presents a unique testbed for formation and dynamical evolution investigations. To facilitate these, it is important to know the masses and orbital elements of all four of the known planets in the system. Although the gas giants in our local solar system have nearly circular and coplanar orbits, this might not be the case for those around HR 8799. Recent fitting attempts to the astrometry from various observatories by other authors have shown evidence that the planets may orbit in planes mutually inclined to one another. Additionally, planet d was found to have a nonzero eccentricity to greater than 1σ confidence. To investigate this I have performed fitting to the Keck self-consistent astrometric data set using Markov Chain Monte Carlo (MCMC). The resulting posterior probability distributions indicate that all four planets may instead orbit in planes with small mutual inclinations ($\lesssim 5^\circ$) about a common plane inclined by $35^\circ \pm 4.4$. While the solutions to all four planets are consistent with circular, planet c had the strongest possibility of a nonzero eccentricity, with a 68% confidence in $e > 0.08$. These findings demonstrate the advantages of using MCMC to explore the parameter space and the comparative differences between the fits to different data sets.

4.1 Motivation to Study the HR 8799 Multi-Planet System

The HR 8799 system has been a popular target for various investigations to better understand exoplanets. Sub-millimeter and infrared observations indicate the system hosts a warm inner dust belt, a cold outer belt and an extended halo [23, 132, 167, 176]. In addition, the system has four known giant planets in wide orbits discovered by high-contrast imaging (HR 8799bcde Marois et al. [127, 129]), an example of a reduced image of the system can be seen in Figure 4.1. This exciting system was shown in terms of stellar flux by Marois et al. [129] to be a "scaled up" version of our own Solar System, although with no inner rocky planets detected as of yet. Being a hot 1.52 $M_{\odot}$ star [9], HR 8799 has few observable spectral lines, all broadened by its rapid rotation, making it impossible to search for any inner rocky planets the system may host with radial velocity measurements.

As the only directly imaged multi-planet system, HR 8799 presents a unique opportunity for investigating formation and dynamical evolution scenarios including migration, planet-planet and planet-disk interaction mechanisms. Theoretical stellar evolutionary tracks, asteroseismology and infrared debris disk modelling predict a wide range of possible ages ($\sim$ 26–1625 Myr) for HR 8799 [37, 140, 146, 172]. However, based on its probable membership in the Columba association [52, 199] and its location on the Hertzsprung-Russell diagram, it is likely $\sim$ 30 Myr [129, 163]. At an age of $\sim$30 Myr, the observed planet luminosities [46, 129, 177] and dynamical stability [77, 142] arguments suggest masses of 5–7 M_{J} for the planets.

To facilitate many of the interesting formation and evolution investigations, a key necessity is the accurate estimation of the orbital parameters for each planet. For directly imaged systems, the short relative coverage of observations over the predicted orbital period complicates attempts to fit the full set of orbital parameters. In these situations a common approach is to reduce the number of orbital elements by fixing some a priori; a few of the typical assumptions are that the orbit is circular, face-on or edge-on, or that the planets are in a mean motion resonance. In the case of HR 8799, recent fitting [eg. 104, 160, 200] has indicated that strictly circular, face-on or even coplanar assumptions might all be invalid. In fact, many [including: 18, 48, 59, 104, 121, 160, 200] have suggested that the orbital plane of planet d could be inclined with respect to other three, and planet d could have a nonzero eccentricity. With the goal of resolving this, Konopacky et al. [104, hereafter K16] suggested the use of a self-consistent astrometric data set. To complement their Monte Carlo exploration of the parameter space, I investigate the possibility of non-coplanarity with my own MCMC analysis. To perform the fitting I will use a new software suite, the Exoplanet Simple Orbit Fitting Toolbox (ExoSOFT) (ExoSOFT; K. Mede & T. Brandt 2016, submitted).

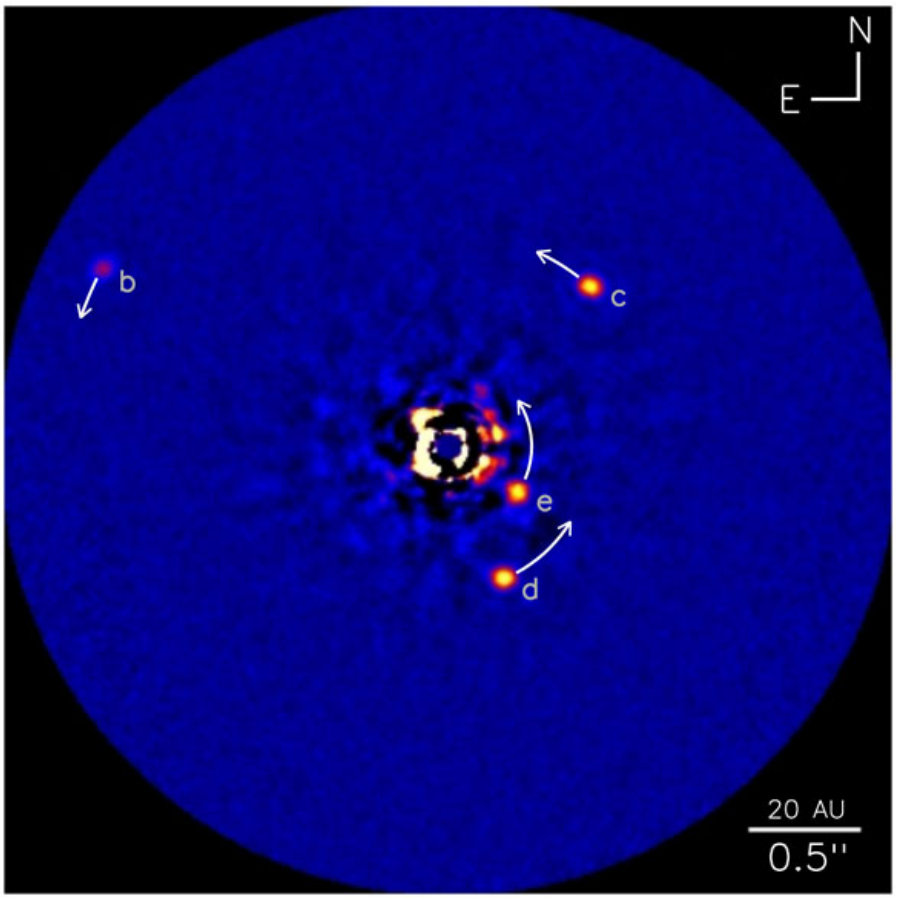

Figure 4.1 Image of all four confirmed planets orbiting HR 8799, together with arrows indicating their projected motion between 2010–2020 based on the nominal fits of Marois et al. [129]. Credit: NRC-HIA, C. Marois & Keck Observatory.

4.2 Fitting

I performed the fitting of the astrometric data using the new software package ExoSOFT (ExoSOFT; K. Mede & T. Brandt 2016, submitted). When provided with only astrometry, the Keplerian model of ExoSOFT has the directly varied parameters $m_{\rm total}$, e, P, ϖ, T_0, i, Ω, ω; respectively these are, the total mass of the system, eccentricity, period, parallax, time of last periapsis, inclination, longitude of the ascending node and the argument of periapsis. To overcome the difficulties that could arise when fitting these 8 parameters with direct sampling methods such as simple Monte Carlo, ExoSOFT employs a multi-stage exploration of the parameter space ending in MCMC. Although for HR 8799 there are no suitable radial velocity data, the software is capable of performing joint fitting to astrometry and radial velocity data simultaneously. Additionally, the package also offers automated post-processing and plotting utilities to summarize the results. Due to the computational complexity of the Keplerian model, it was written in the C++ programming language while the majority of the code was written in Python.

Table 4.1. The Eccentricity and Inclination of HR 8799bcde

	b	c	d	e
e ( ) median	0.206	0.139	0.171	0.122
1σ range[a]	[0,0.31]	[0,0.21]	[0,0.31]	[0,0.17]
i (°) median	35.2	28.6	37.6	24.5
1σ range[a]	[27.9,47.2]	[19.3,42.0]	[29.4,50.0]	[11.5,36.7]
χ^2 (ν)[b]	7.30 (20)	6.33 (20)	15.4 (18)	5.61 (12)

[a] Approximate 1σ uncertainty: 68.3% of the posterior probability lies in this range

[b] ν represents the number of degrees of freedom during MCMC joint fitting: ν=(# epochs)(2 dimensions)−(6 varied params), where the number of epochs are 13, 13, 12, 9 for b, c, d, and e, respectively.

As each planet's orbit was computed separately, I assumed a fixed total system mass (equal to that of the primary star) and neglected the perturbations from the other planets. The recent mass estimates for HR 8799 by Baines et al. [9] are $1.513^{+0.023}_{-0.024}$ $M_\odot$ for an age of 90^{+381}_{-50}Myr, or $1.516^{+0.038}_{-0.024}$ $M_\odot$ for $33^{+7}_{-13.2}$Myr. Without an independent age estimate I used $m_{\rm total} = 1.51 M_\odot$, well within both 1σ uncertainties. With the planets having masses on the order of 5–10 M_J (0.005–0.01 $M_\odot$), their influence on the value of $m_{\rm total}$ is smaller than the uncertainties of m_1. Similarly, the parallax was fixed to that of van Leeuwen [189] (39.4 pc) when converting the model separation values in AU to that of arc seconds in the measured astrometry. With the focus of this work on the inclination and eccentricity values, the choice to fix these parameters is supported by the fact that they will not affect the resulting posterior probability distributions for those parameters. With the total mass and parallax fixed, the varied parameters of ExoSOFT's Keplerian model are (e, P, T_0, i, Ω, ω). The samples for these were drawn from uniform proposal distributions. Uniform priors were given to e, T_0, Ω and ω, while i and P were given the priors $p(i) \propto \cos(i)$ and $p(P) \propto 1/P$, respectively.

For each of the planets, 160 Markov chains of 2×10^8 samples each were run, storing only every 20,000$^{\rm th}$ step to reduce the number of correlated samples in the final data set. The chain convergence was measured using the Gelman-Rubin statistic, for which a value of 1.01 translates to a convergence to the posterior probability distributions with a precision of 1%. For the inclination and eccentricity parameters, only those of planet e reached convergence values of < 1.01, while those of the other three planets had at best a precision of 10%.

The results for the inclination and eccentricity posterior probability distributions for all four planets are shown in Figure 4.2, and summarized in Table 4.1. The best fitting orbits along with their associated measured astrometry can be seen in Figure 4.3. As not all the MCMC chains fully converged their results must be considered preliminary. The choice here to only use the self consistent

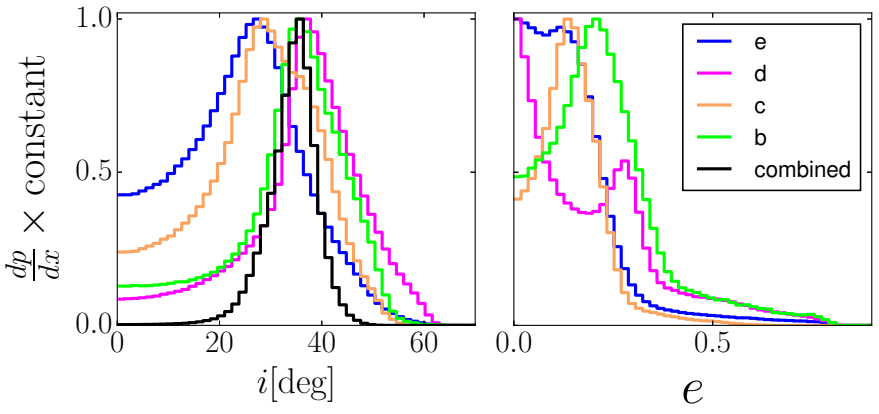

Figure 4.2 The posterior probability distributions for inclination and eccentricity of planets HR 8799bcde, using the original astrometric uncertainties from K16. The black line in the inclination posteriors panel represents the combined distribution for all four planets produced by multiplying each planets' distribution together.

data set from Keck presented in K16 follows from their suggestion and the comments in Pueyo et al. [160, hereafter P15]; P15 noted that the calibration differences between observatories (eg. true north, distortion, or plate scale) and those due to different data reduction pipelines can bring about unaccounted uncertainties that may lead to disproportionate weightings between the data sets of said observatories.

4.3 Results and Discussion

Many authors have previously fit the orbits of the planets in the HR 8799 system, including Bergfors et al. [18], Currie et al. [48], Esposito et al. [60], Fabrycky & Murray-Clay [62], Goździewski & Migaszewski [77], Konopacky et al. [104], Maire et al. [121], Marois et al. [129], Pueyo et al. [160], Soummer et al. [173], Zurlo et al. [200]. In all cases the short orbital coverage of the available astrometry has limited their ability to draw conclusive statements about the coplanarity or eccentricities. The difficulty to fit the full set of orbital elements has led some to assume the orbits of all four planets are coplanar, circular and/or reside in a hierarchy of mean motion resonance [eg. 48, 59, 62, 121, 127, 129, 200]. Two of the most recent fitting efforts in P15 and K16 performed a largely open parameter space exploration in order to investigate the validity of those assumptions. While both studies find the system to be consistent with circular, coplanar orbits, P15 in particular found that planet d could be misaligned by $\sim$ 15–20° to the other three, and might also have an eccentricity of ~ 0.26. The results of the MCMC fitting with ExoSOFT to the self-consistent data set of K16 presented here complement previous fitting work by other authors.

While the nominal fitting solutions for the HR 8799 planets presented in Marois et al. [129] assumed only face-on orbits, some have allowed the inclination parameter to remain open. The most recent papers to permit all inclination values are P15 and K16, which used different parameter space exploration approaches and different astrometric data sets. A summary of the most comparable solutions from this work, together with those from P15 and K16 can be found in Table 4.2. Compared to that of P15, those of bcd are 10–18° higher for both the ExoSOFT and K16 fits. In fact, as the fitting presented here was performed with the same self-consistent data set as K16, the resulting median values lie within their respective 1σ ranges for planets bcd. Thus, the solution divergences in the inclination fits for bcd are most likely due to the use of different astrometric data in P15. As per planet e, both the median values in Table 4.1 and the those in P15 are $\sim 25°$. Although the unweighted Monte Carlo inclination distribution shown in figure 7 of K16 for planet e is peaked close to 48°, their results when only considering orbits that do not pass within the Hill radius of another planet had a peak for planet e around 30°. Overall, this implies the results for planet e from K16, P15 and that here all give values of about 25–35°, and those for bcd differ most likely due to the different data sets being used by P15.

The inclination posteriors for the planets in Figure 4.2 share a region with simultaneous confidence greater than 1σ ([25.1,35.8]), suggesting a common orbital plane with small mutual inclinations. Assuming the planets orbit in a common plane, the distribution of possible inclinations for said plane

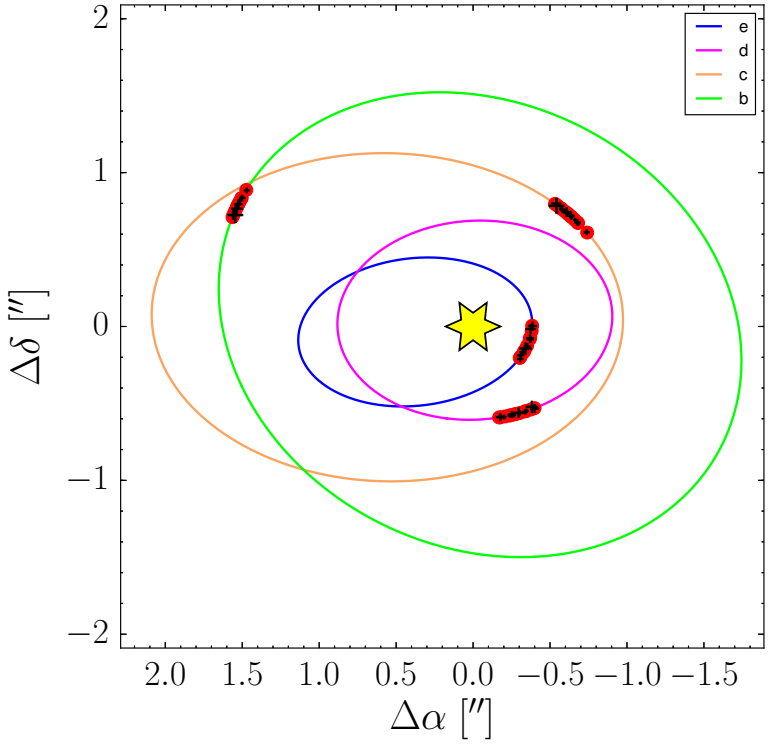

Figure 4.3 Measured astrometry for planets HR 8799bcde atop their best-fitting orbits. Both the outer two and inner two planets show overlapping orbits. To remain stable, such configurations require mean motion resonance (MMR). As planet-planet interactions were neglected and no MMR requirements were placed a priori, the plotted orbital configuration is most likely unstable. A dynamical stability analysis would confirm this, but is beyond the scope of this paper.

Table 4.2. Inclinations of HR 8799bcde From This Work and Recent Papers

	b	c	d	e
i (°) K16[a]	38	37	45	48
i (°) P15[b]	17.2	10.5	26.3	25.5
i (°) median [original]*	35.2	28.6	37.6	24.5
1σ range[c]	[27.9,47.2]	[19.3,42.0]	[29.4,50.0]	[11.5,36.7]
i (°) median [scaled]**	37.1	30.2	39.0	26.0
1σ range[c]	[32.1,42.5]	[23.7,39.3]	[31.9,49.8]	[15.9,37.0]

[a] Unweighted distribution peak locations determined through visual inspection of figures 4-7 in Konopacky et al. [104] (K16)

[b] Values with the highest likelihood from table 3 in Pueyo et al. [160] (P15)

[c] Approximate 1σ uncertainty: 68.3% of the posterior probability lies above this range

* Median fit values using the original astrometric uncertainties reported in K16

** Median fit values using the astrometric uncertainties reported in K16, rescaled by a constant factor to yield a best-fit $\chi^2_\nu = 1$

can be represented by the product of the individual planet posteriors, shown as the black line in the left panel of Figure 4.2, having a median value of 35° and a 1σ confidence region of [30.4,39.2]. While the limited orbital coverage leads to distributions for the inclinations with inconclusive results for the planets on their own, the combined posterior does allow for some interesting comparisons to be made. A contrasting approach to investigating coplanarity in K16 involved fixing the inclination of all four planets to values drawn from the posterior of planet b's inclination and re-performing their Monte Carlo fitting. Their posterior for the inclination of planet b has a closely matching median of 38° and is visually similar to the combined posterior in Figure 4.2. The median value of 35° for the combined posterior also falls within the range of inclination estimates from modeling the outer disk, for which Booth et al. [23], Matthews et al. [132], and Su et al. [176] suggest values between 23–45°. Additionally, if the planets orbit in a common plane near $i \approx 35°$, then this plane is within a few degrees of the lower limits placed on the rotational plane of HR 8799 itself by asteroseismology; those being >40° in Wright et al. [196] and >36° in Moya et al. [146]. Even given that this is a preliminary result, it suggests that the disk, planets and stellar rotational plane are all aligned.

The requirement of circular orbits was lifted in the same recent fitting work by P15 and K16. Similar to that of the inclination, the results from the ExoSOFT fitting are unable to make conclusive statements about the eccentricities of the planets, with the solutions all having non-negligible likelihoods of being circular. At the same time, it is not strictly expected that giant planets on wide orbits would be in purely circular orbits as even those of Jupiter and Saturn have e$\sim$ 0.05. Upon inspection, the

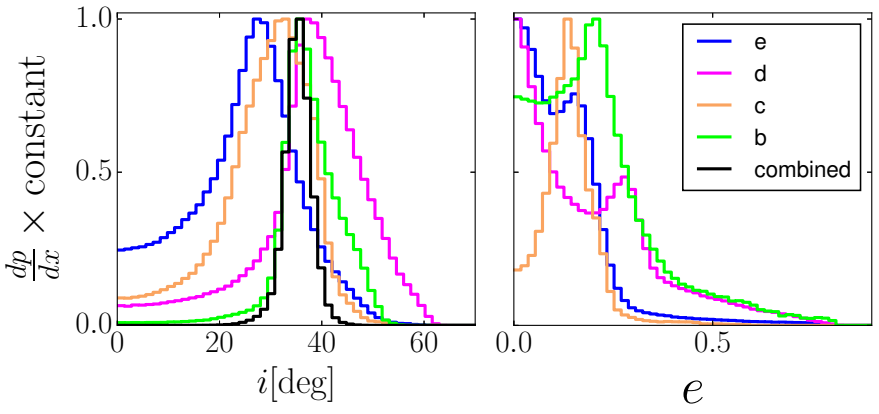

Figure 4.4 The posterior probability distributions for inclination and eccentricity of planets HR 8799bcde, using error values deflated in quadrature to produce best fit $\chi^2_\nu \sim 1$. The black line in the inclination posteriors panel represents the combined distribution for all four planets.

eccentricity distributions in Figure 4.2 appear to be more well-sampled versions of those given in figure 9 of K16, most likely arising from the use of the same data set coupled with an MCMC parameter exploration approach.

The low χ^2_ν values in Table 4.1 reveal a possible overestimation of the astrometric uncertainties. Such errors can propagate into the posterior probability distributions, artificially broadening them. To better understand their effect, I rescaled the errors in K16 by a constant factor to yield a best-fit $\chi^2_\nu = 1$; specifically, the errors for each planet's astrometric data were multiplied by (0.604, 0.563, 0.925, 0.684) for (b, c, d, e). For comparison, the resulting inclination distribution values are summarized in Table 4.2 together with those from Table 4.1, and the most similar values reported in P15 and K16. As can be seen in Figure 4.4, the distributions are generally more narrow than those with the original uncertainties. In fact, their 1σ confidence regions decreased in width by 14–46%, with that of planet b decreasing the most. The eccentricity distributions in the right panel of Figure 4.4 are similar to those in Figure 4.2, with planet c showing the strongest likelihood of a nonzero eccentricity, having a 68% confidence in $e > 0.08$. Even though the parameter distributions are tighter, the MCMC chains did not fully converge, making it impossible to draw strong conclusions about the system's coplanarity or eccentricities for either set of astrometric uncertainties.

As discussed earlier, although the combined inclination posterior has a median value similar to those of the outer disk and equator of HR 8799 itself, each planet's inclination posterior has a non-negligible width. Should their orbits in fact be mutually inclined, the N-body simulations of Veras et al. [191] showed that the average inclinations between planets in multi-planet systems decrease from the ages of 10 to 500 Myr by ∼19%. With the small mutual inclinations found here, this suggests the system may have formed close to its current state. Similarly, Sudol & Haghighipour [177] found coplanar solutions to the orbits of all 4 planets inclined by 30° that remained dynamically stable up to 155 Myr, near the upper limit of HR 8799's age estimate (160 Myr) in Marois et al. [127].

As can be seen in Figure 4.3, the best-fit orbits of both the inner and outer two planets cross in the plane of the sky. For the HR 8799 system, Fabrycky & Murray-Clay [62] were first to suggest that for orbits in such a configuration to remain dynamically stable, their periods would have to be locked in a mean motion resonance. In fact, they showed that the nominal orbital solutions in the HR 8799bcd discovery paper [127] are dynamically unstable. Along the same lines, the high masses of the planets in the system would also suffer from instabilities arising from large libration widths, also referred to as mean motion resonance overlaps [111, 143]. This was presented as the primary driver for instability in Morrison & Kratter [143], with the misalignment of the orbital planes suggested as the best way to recover system stability. Interestingly, they argued that "resonance can both stabilize and destabilize systems, while misaligned orbital planes will likely enhance stability". Therefore, while the results shown here are incapable of proving or disproving misalignment, they do importantly suggest that any mutual inclinations would be small ($\lesssim 10°$).

4.4 Summary and Future of HR 8799bcde Orbit Fitting

The HR 8799 planetary system has received a high level of attention since its discovery in Marois et al. [127]. Following this, fitting to subsequent astrometry has caused some to argue that the orbits of the four giant planets in the system might be eccentric and reside in different planes. To investigate these, I fit the orbital elements for each planet separately, using the self consistent data set from the Keck Observatory and the MCMC parameter space exploration capabilities of ExoSOFT.

The inclination posterior probability distributions have a modest spread of median values for each of the four planets, but overlapping 1σ confidence regions suggest coplanarity. If the system is coplanar, it would have an inclination of $35°^{+4.2}_{-4.6}$ or $35°^{+2.9}_{-2.1}$, for the original and scaled astrometric uncertainties. This proposed orbital plane for the planets would then lie near those predicted for the outer disk and the rotational plane of the host star itself. When fitting to the astrometric data with scaled uncertainties, all four planets are consistent with circular orbits at the 95% confidence level. For the same scaled data set, the posterior probability distribution of planet c was the most suggestive of a nonzero eccentricity, having a 68% confidence in $e > 0.08$.

With their long orbital periods and only astrometric data available, the ability to strongly constrain the orbital parameters of the HR 8799 planets is likely to remain a difficult task for many years to come. This could be accomplished in a shorter time frame should data acquired from radial velocity measurements also show a clear detection of all four planets. Unfortunately, the high temperature and rotation speed of HR 8799 make it impossible to disentangle any planetary radial velocity signal from the few available broad lines in its spectrum. Therefore, continued astrometric monitoring of the system is the only manner to better constrain its coplanarity and eccentricities. Independent to the acquisition of new astrometry, or what data sets are used, the capabilities of ExoSOFT make it a suitable choice to investigate the orbital parameter space of this exciting planetary system.

Chapter 5

Conclusion

In this thesis I presented ExoSOFT and its application to the V450 Andromedae and HR 8799 systems.

First, in Chapter 1 I reviewed the status of the field of exoplanet research, the methods to find exoplanets with both direct and indirect detection techniques, and the important scientific questions about exoplanet formation and evolution currently being investigated. With many of these questions benefiting from accurate estimates of the systems' orbital elements and dynamical masses, I developed the Exoplanet Simple Orbit Fitting Toolbox (ExoSOFT) to help solve for these values by fitting measured radial velocity and astrometric data to a Keplerian model. The details of the Keplerian model, the methods to explore its possibly complicated parameter space and a verification of the software was given in Chapter 2. Once fully verified, ExoSOFT was then used in investigations of the companions to both V450 Andromedae and HR 8799, in Chapters 3 and 4, respectively.

ExoSOFT is an open source toolbox for fitting the Keplerian orbital elements of binary stars and exoplanets using any combination of radial velocity and astrometric data. To overcome the computational difficulties that arise when trying to sample the possibly complicated parameter space of Keplerian models, ExoSOFT follows a suggested 3 stage exploration approach ending in MCMC. It implements Simulated Annealing and Sigma Tuning to solve for suitable starting positions and perform necessary sampling optimizations. With these complete, long runs of MCMC can be carried out until convergence to the posterior probability distributions is achieved. To summarize the results, I have packaged ExoSOFT together with a suite of plotting and statistical analysis utilities.

I used the particular joint analysis capabilities of ExoSOFT to investigate the complete orbital solution of the companion to V450 Andromedae. By taking advantage of a broader radial velocity coverage and the first detections with high contrast imaging, I was able to break the $\sin(i)$ degeneracy of earlier investigations. Our work showed the companion to in fact be a $0.282^{+0.042}_{-0.023}$ M$\odot$ star on a nearly face-on, eccentric orbit, isolating the mass from the previously estimated $m_2 \sin(i) \approx 52$ M$_\mathrm{J}$, and showing the companion to be stellar. This work demonstrates the benefits of utilizing multiple observables, when possible, to break model degeneracies.

In addition, I performed MCMC fitting of the 4 known planetary mass companions orbiting HR 8799 with a self-consistent data set from the Keck Observatory. While preliminary, the resulting posterior probability distributions support the planets having circular orbits, with only planet c showing to greater than 68% confidence that its eccentricity is $e > 0.08$. No strong evidence was found supporting planet d having a high mutual inclination with respect to the other three, as other authors had indicated. In fact, the inclination posteriors instead showed a possibility that all four planets orbit within 5° of a common plane inclined by $35° \pm 4.4$, similar to the orbital plane of the outer disk and the rotational equator of HR 8799 itself.

The investigations presented here for the V450 Andromedae and HR 8799 systems showcase the importance of attaining high precision data and employing multiple observables when possible. Upcoming space and ground-based missions will dramatically expand the number of systems observed with both astrometric and radial velocity instruments. In fact, even with current transit data, Dressing & Charbonneau [53] found a cumulative occurrence rate of 2.5 small (<4 $R_\oplus$) planets around an average M dwarf star. Similarly, revised estimates by Perryman et al. [154] predict that if *Gaia* operates for its entire expected lifetime it could find up to 70,000 giant planets. Together, *Gaia* astrometry and precision radial velocity follow-up observations will answer key questions about planetary formation. In order to understand these data, we need advanced software tools to solve for the orbital elements and dynamical masses of the exoplanets observed. With these important investigations on the horizon, the joint fitting capabilities and open source design will make ExoSOFT an increasingly useful tool for the astronomical community.

Bibliography

[1] Albrecht, S., Winn, J. N., Butler, R. P., et al. 2012, ApJ, 744, 189

[2] Allard, F. 1990, Ph.D. thesis, Centre de Recherche Astrophysique de Lyon

[3] Ambartsumian, V. A. 1937, AZh, 14, 207

[4] Apai, D., Kasper, M., Skemer, A., et al. 2016, ApJ, 820, 40

[5] Artigau, É., Donati, J.-F., & Delfosse, X. 2011, in Astronomical Society of the Pacific Conference Series, Vol. 448, 16th Cambridge Workshop on Cool Stars, Stellar Systems, and the Sun, ed. C. Johns-Krull, M. K. Browning, & A. A. West, 771

[6] Artigau, É., Kouach, D., Donati, J.-F., et al. 2014, in Proc. SPIE, Vol. 9147, Ground-based and Airborne Instrumentation for Astronomy V, 914715

[7] Asada, H. 2008, PASJ, 60, 843

[8] Bailes, M., Bates, S. D., Bhalerao, V., et al. 2011, Science, 333, 1717

[9] Baines, E. K., White, R. J., Huber, D., et al. 2012, ApJ, 761, 57

[10] Bakos, G., Noyes, R. W., Kovács, G., et al. 2004, PASP, 116, 266

[11] Balan, S. T., & Lahav, O. 2009, MNRAS, 394, 1936

[12] Baraffe, I., Chabrier, G., Barman, T. S., Allard, F., & Hauschildt, P. H. 2003, A&A, 402, 701

[13] Batalha, N. M., Rowe, J. F., Bryson, S. T., et al. 2013, ApJS, 204, 24

[14] Bate, M. R. 2009, MNRAS, 392, 590

[15] Bate, M. R., Bonnell, I. A., & Bromm, V. 2003, MNRAS, 339, 577

[16] Beaulieu, J.-P., Bennett, D. P., Fouqué, P., et al. 2006, Nature, 439, 437

[17] Becklin, E. E., & Zuckerman, B. 1988, Nature, 336, 656

[18] Bergfors, C., Brandner, W., Janson, M., Köhler, R., & Henning, T. 2011, A&A, 528, A134

[19] Beuzit, J.-L., Feldt, M., Dohlen, K., et al. 2008, in Proc. SPIE, Vol. 7014, 18

[20] Boley, A. C. 2009, ApJ, 695, L53

[21] Bonfils, X., Delfosse, X., Udry, S., et al. 2013, A&A, 549, A109

[22] Bonnefoy, M., Zurlo, A., Baudino, J. L., et al. 2016, A&A, 587, A58

[23] Booth, M., Jordán, A., Casassus, S., et al. 2016, MNRAS, 1603.04853

[24] Boss, A. P. 1997, Science, 276, 1836

[25] Bouchy, F., Hébrard, G., Udry, S., et al. 2009, A&A, 505, 853

[26] Braak, C. J. F. T. 2006, Statistics and Computing, 16, 239

[27] Brandt, T. D., McElwain, M. W., Turner, E. L., et al. 2013, ApJ, 764, 183

[28] Brandt, T. D., McElwain, M. W., Turner, E. L., et al. 2014, ApJ, 794, 159

[29] Cameron, A. G. W. 1978, Moon and Planets, 18, 5

[30] Casertano, S., Lattanzi, M. G., Sozzetti, A., et al. 2008, A&A, 482, 699

[31] Chabrier, G. 2003a, PASP, 115, 763

[32] Chabrier, G. 2003b, PASP, 115, 763

[33] Chabrier, G., & Baraffe, I. 2000, ARA&A, 38, 337

[34] Chabrier, G., Johansen, A., Janson, M., & Rafikov, R. 2014, Protostars and Planets VI, 619

[35] Chatterjee, S., Ford, E. B., Matsumura, S., & Rasio, F. A. 2008, ApJ, 686, 580

[36] Chauvin, G., Lagrange, A.-M., Dumas, C., et al. 2004, A&A, 425, L29

[37] Chen, C. H., Sargent, B. A., Bohac, C., et al. 2006, ApJS, 166, 351

[38] Claudi, R. U., Turatto, M., Antichi, J., et al. 2006, in Proc. SPIE, Vol. 6269, Society of Photo-Optical Instrumentation Engineers (SPIE) Conference Series, 62692Y

[39] Crepp, J. R., Johnson, J. A., Fischer, D. A., et al. 2012a, ApJ, 751, 97

[40] Crepp, J. R., Johnson, J. A., Fischer, D. A., et al. 2012b, ApJ, 751, 97

[41] Crepp, J. R., Johnson, J. A., Howard, A. W., et al. 2014, ApJ, 781, 29

[42] Crepp, J. R., Johnson, J. A., Howard, A. W., et al. 2012c, ApJ, 761, 39

[43] Crepp, J. R., Johnson, J. A., Howard, A. W., et al. 2013a, ApJ, 771, 46

[44] Crepp, J. R., Johnson, J. A., Howard, A. W., et al. 2013b, ApJ, 774, 1

[45] Cumming, A., Butler, R. P., Marcy, G. W., et al. 2008, PASP, 120, 531

[46] Currie, T., Burrows, A., Itoh, Y., et al. 2011, The Astrophysical Journal, 729, 128

[47] Currie, T., Daemgen, S., Debes, J., et al. 2014, ApJ, 780, L30

[48] Currie, T., Fukagawa, M., Thalmann, C., Matsumura, S., & Plavchan, P. 2012, ApJ, 755, L34

[49] David, T. J., Hillenbrand, L. A., Petigura, E. A., et al. 2016, ArXiv e-prints, 1606.06729

[50] Deitrick, R., Barnes, R., McArthur, B., et al. 2015, ApJ, 798, 46

[51] Dodson-Robinson, S. E., Veras, D., Ford, E. B., & Beichman, C. A. 2009, ApJ, 707, 79

[52] Doyon, R., Lafrenière, D., Artigau, E., Malo, L., & Marois, C. 2010, in In the Spirit of Lyot 2010

[53] Dressing, C. D., & Charbonneau, D. 2015, ApJ, 807, 45

[54] Duquennoy, A., & Mayor, M. 1991a, A&A, 248, 485

[55] Duquennoy, A., & Mayor, M. 1991b, A&A, 248, 485

[56] Eastman, J., Gaudi, B. S., & Agol, E. 2013, PASP, 125, 83

[57] Eastman, J. D., Brown, T. M., Hygelund, J., et al. 2014, in Proc. SPIE, Vol. 9147, Ground-based and Airborne Instrumentation for Astronomy V, 914716

[58] Egner, S., Ikeda, Y., Watanabe, M., et al. 2010, in Proc. SPIE, Vol. 7736, 4

[59] Esposito, S., Mesa, D., Skemer, A., et al. 2013, A&A, 549, A52

[60] Esposito, S., Riccardi, A., Pinna, E., et al. 2011, in Society of Photo-Optical Instrumentation Engineers (SPIE) Conference Series, Vol. 8149

[61] Evans, T. M., Ireland, M. J., Kraus, A. L., et al. 2012, ApJ, 744, 120

[62] Fabrycky, D. C., & Murray-Clay, R. A. 2010, ApJ, 710, 1408

[63] Feroz, F., Hobson, M. P., & Bridges, M. 2009, MNRAS, 398, 1601

[64] Fischer, D. A., Anglada-Escude, G., Arriagada, P., et al. 2016, PASP, 128, 066001

[65] Fischer, D. A., Marcy, G. W., & Spronck, J. F. P. 2014, ApJS, 210, 5

[66] Fonnesbeck, C., Patil, A., Huard, D., & Salvatier, J. 2015, PyMC: Bayesian Stochastic Modelling in Python, Astrophysics Source Code Library

[67] Ford, E. B. 2005, AJ, 129, 1706

[68] Ford, E. B. 2006, ApJ, 642, 505

[69] Ford, E. B., & Rasio, F. A. 2008, ApJ, 686, 621

[70] Foreman-Mackey, D., Hogg, D. W., Lang, D., & Goodman, J. 2013, PASP, 125, 306

[71] Forveille, T., Beuzit, J.-L., Delfosse, X., et al. 1999, A&A, 351, 619

[72] Gaudi, B. S. 2012, ARA&A, 50, 411

[73] Gelman, A., Roberts, G., & Gilks, W. 1996, Bayesian Statistics, 5, 599

[74] Gelman, A., & Rubin, D. B. 1992, Statist. Sci., 7, 457

[75] Goldreich, P., & Ward, W. R. 1973, ApJ, 183, 1051

[76] Goździewski, K., & Migaszewski, C. 2009, MNRAS, 397, L16

[77] Goździewski, K., & Migaszewski, C. 2014, MNRAS, 440, 3140

[78] Gregory, P. 2005, Bayesian Logical Data Analysis for the Physical Sciences: A Comparative Approach with Mathematica® Support (Cambridge University Press)

[79] Gregory, P. C. 2005, ApJ, 631, 1198

[80] Grether, D., & Lineweaver, C. H. 2006, ApJ, 640, 1051

[81] Grossman, A. S., Hays, D., & Graboske, H. C., Jr. 1974, A&A, 30, 95

[82] Han, E., Wang, S. X., Wright, J. T., et al. 2014, PASP, 126, 827

[83] Hartkopf, W. I., McAlister, H. A., & Franz, O. G. 1989, AJ, 98, 1014

[84] Hashimoto, J., Dong, R., Kudo, T., et al. 2012, ApJ, 758, L19

[85] Hastings, W. 1970, Biometrika, 57, 97

[86] Hayano, Y., Takami, H., Oya, S., et al. 2010, in Proc. SPIE, Vol. 7736, 0

[87] Hayashi, C. 1981, Progress of Theoretical Physics Supplement, 70, 35

[88] Hebrard, G., Arnold, L., Forveille, T., et al. 2016, ArXiv e-prints, 1602.04622

[89] Heintz, W. 1978, Double stars, Geophysics and astrophysics monographs (D. Reidel Pub., Co.)

[90] Hełminiak, K. G., Kuzuhara, M., Mede, K., et al. 2016, ApJ

[91] Helled, R., Bodenheimer, P., Podolak, M., et al. 2014, Protostars and Planets VI, 643

[92] Hinkley, S., Pueyo, L., Faherty, J. K., et al. 2013, ApJ, 779, 153

[93] Hogg, D. W., Myers, A. D., & Bovy, J. 2010, ApJ, 725, 2166

[94] Ida, S., & Lin, D. N. C. 2004, ApJ, 604, 388

[95] Iglesias-Marzoa, R., López-Morales, M., & Jesús Arévalo Morales, M. 2015, PASP, 127, 567

[96] Ingraham, P., Marley, M. S., Saumon, D., et al. 2014, ApJ, 794, L15

[97] Janson, M., Brandt, T. D., Kuzuhara, M., et al. 2013, ApJ, 778, L4

[98] Jovanovic, N., Martinache, F., Guyon, O., et al. 2015, PASP, 127, 890

[99] Jurić, M., & Tremaine, S. 2008, ApJ, 686, 603

[100] Käufl, H. U., Amico, P., Ballester, P., et al. 2008, in Proc. SPIE, Vol. 7014, Ground-based and Airborne Instrumentation for Astronomy II, 70140W

[101] Kipping, D. M. 2013, MNRAS, 434, L51

[102] Kipping, D. M., & Sandford, E. 2016, ArXiv e-prints, 1603.05662

[103] Kirkpatrick, S., Gelatt, C. D., & Vecchi, M. P. 1983, Science, 220, 671

[104] Konopacky, Q. M., Marois, C., Macintosh, B. A., et al. 2016, ArXiv e-prints, 1604.08157

[105] Kozai, Y. 1962, AJ, 67, 591

[106] Kratter, K. M., Murray-Clay, R. A., & Youdin, A. N. 2010, ApJ, 710, 1375

[107] Kreidberg, L. 2015, PASP, 127, 1161

[108] Kui, R. 1991, Ph.D. thesis, PhD. thesis. Natl. Univ. Aust. , (1991)

[109] Kuiper, G. P. 1951, Proceedings of the National Academy of Science, 37, 1

[110] Lagrange, A.-M., Gratadour, D., Chauvin, G., et al. 2009, A&A, 493, L21

[111] Lecar, M., Franklin, F. A., Holman, M. J., & Murray, N. J. 2001, ARA&A, 39, 581

[112] Levenberg, K. 1944, Quarterly of Applied Mathematics, 2, 164

[113] Lidov, M. L. 1962, Planet. Space Sci., 9, 719

[114] Liu, J. S. 2008, Monte Carlo Strategies in Scientific Computing (Corrected ed.) (Springer)

[115] Liu, M. C., Dupuy, T. J., & Ireland, M. J. 2008, ApJ, 689, 436

[116] Low, C., & Lynden-Bell, D. 1976, MNRAS, 176, 367

[117] Macintosh, B., Graham, J. R., Ingraham, P., et al. 2014a, Proceedings of the National Academy of Science, 111, 12661

[118] Macintosh, B. A., Anthony, A., Atwood, J., et al. 2014b, in Proc. SPIE, Vol. 9148, Adaptive Optics Systems IV, 91480J

[119] Madhusudhan, N., Agúndez, M., Moses, J. I., & Hu, Y. 2016, Space Sci. Rev., 1604.06092

[120] Mahadevan, S., Ramsey, L., Bender, C., et al. 2012, in Proc. SPIE, Vol. 8446, Ground-based and Airborne Instrumentation for Astronomy IV, 84461S

[121] Maire, A.-L., Skemer, A. J., Hinz, P. M., et al. 2015, A&A, 576, A133

[122] Mandel, K., & Agol, E. 2002, ApJ, 580, L171

[123] Marcy, G. W., & Butler, R. P. 1992, PASP, 104, 270

[124] Marcy, G. W., & Butler, R. P. 2000, PASP, 112, 137

[125] Marley, M. S., Fortney, J. J., Hubickyj, O., Bodenheimer, P., & Lissauer, J. J. 2007, ApJ, 655, 541

[126] Marois, C., Lafrenière, D., Doyon, R., Macintosh, B., & Nadeau, D. 2006, ApJ, 641, 556

[127] Marois, C., Macintosh, B., Barman, T., et al. 2008a, Science, 322, 1348

[128] Marois, C., Macintosh, B., Barman, T., et al. 2008b, Science, 322, 1348

[129] Marois, C., Zuckerman, B., Konopacky, Q. M., Macintosh, B., & Barman, T. 2010, Nature, 468, 1080

[130] Marquardt, D. W. 1963, Journal of the Society for Industrial and Applied Mathematics, 11, 431

[131] Martinache, F., Guyon, O., Jovanovic, N., et al. 2014, PASP, 126, 565

[132] Matthews, B., Kennedy, G., Sibthorpe, B., et al. 2014, ApJ, 780, 97

[133] McArthur, B. E., Benedict, G. F., Barnes, R., et al. 2010, ApJ, 715, 1203

[134] Mede, K., & Brandt, T. D. 2014, in IAU Symposium, Vol. 299, IAU Symposium, ed. M. Booth, B. C. Matthews, & J. R. Graham, 52

[135] Meschiari, S., Wolf, A. S., Rivera, E., et al. 2009, PASP, 121, 1016

[136] Metchev, S. A., & Hillenbrand, L. A. 2009a, ApJS, 181, 62

[137] Metchev, S. A., & Hillenbrand, L. A. 2009b, ApJS, 181, 62

[138] Metropolis, N., Rosenbluth, A. W., Rosenbluth, M. N., Teller, A. H., & Teller, E. 1953, J. Chem. Phys., 21, 1087

[139] Mizuno, H. 1980, Progress of Theoretical Physics, 64, 544

[140] Moór, A., Ábrahám, P., Derekas, A., et al. 2006, ApJ, 644, 525

[141] Mordasini, C., Alibert, Y., Benz, W., Klahr, H., & Henning, T. 2012, A&A, 541, A97

[142] Moro-Martín, A., Rieke, G. H., & Su, K. Y. L. 2010, ApJ, 721, L199

[143] Morrison, S. J., & Kratter, K. M. 2016, ArXiv e-prints, 1604.01037

[144] Mould, J. R. 1976, ApJ, 210, 402

[145] Moultaka, J., Ilovaisky, S., Prugniel, P., & Soubiran, C. 2004, in SF2A-2004: Semaine de l'Astrophysique Francaise, ed. F. Combes, D. Barret, T. Contini, F. Meynadier, & L. Pagani, 547

[146] Moya, A., Amado, P. J., Barrado, D., et al. 2010, MNRAS, 406, 566

[147] Nagasawa, M., & Ida, S. 2011, ApJ, 742, 72

[148] Nagasawa, M., Ida, S., & Bessho, T. 2008, ApJ, 678, 498

[149] Nakajima, T., Oppenheimer, B. R., Kulkarni, S. R., et al. 1995, Nature, 378, 463

[150] Nelson, B., Ford, E. B., & Payne, M. J. 2014, ApJS, 210, 11

[151] Parviainen, H. 2015, MNRAS, 450, 3233

[152] Pepe, F., Cristiani, S., Rebolo, R., et al. 2013, The Messenger, 153, 6

[153] Perrier, C., Sivan, J.-P., Naef, D., et al. 2003, A&A, 410, 1039

[154] Perryman, M., Hartman, J., Bakos, G. Á., & Lindegren, L. 2014, ApJ, 797, 14

[155] Peters, M. A., Groff, T., Kasdin, N. J., et al. 2012, in Society of Photo-Optical Instrumentation Engineers (SPIE) Conference Series, Vol. 8446, 7

[156] Pollacco, D. L., Skillen, I., Collier Cameron, A., et al. 2006, PASP, 118, 1407

[157] Pollack, J. B., Hubickyj, O., Bodenheimer, P., et al. 1996, Icarus, 124, 62

[158] Pourbaix, D. 1998, A&AS, 131, 377

[159] Press, W. 2007, Numerical Recipes 3rd Edition: The Art of Scientific Computing (Cambridge University Press)

[160] Pueyo, L., Soummer, R., Hoffmann, J., et al. 2015, ApJ, 803, 31

[161] Quirrenbach, A., Amado, P. J., Caballero, J. A., et al. 2014, in Proc. SPIE, Vol. 9147, Ground-based and Airborne Instrumentation for Astronomy V, 91471F

[162] Rameau, J., Chauvin, G., Lagrange, A.-M., et al. 2013, ApJ, 772, L15

[163] Rhee, J. H., Song, I., Zuckerman, B., & McElwain, M. 2007, ApJ, 660, 1556

[164] Riddle, R. L., Tokovinin, A., Mason, B. D., et al. 2015, ApJ, 799, 4

[165] Rodriguez, D. R., Zuckerman, B., Melis, C., & Song, I. 2011, ApJ, 732, L29

[166] Ryu, T., Sato, B., Kuzuhara, M., et al. 2016, ArXiv e-prints, 1603.02017

[167] Sadakane, K., & Nishida, M. 1986, PASP, 98, 685

[168] Safronov, V. S., & Zvjagina, E. V. 1969, Icarus, 10, 109

[169] Sato, B., Fischer, D. A., Ida, S., et al. 2009, ApJ, 703, 671

[170] Schulze-Hartung, T., Launhardt, R., & Henning, T. 2012, ArXiv e-prints, 1207.6276

[171] Shabram, M., Demory, B.-O., Cisewski, J., Ford, E. B., & Rogers, L. 2016, ApJ, 820, 93

[172] Song, I., Caillault, J.-P., Barrado y Navascués, D., & Stauffer, J. R. 2001, ApJ, 546, 352

[173] Soummer, R., Hagan, J. B., Pueyo, L., et al. 2011, The Astrophysical Journal, 741, 55

[174] Spiegel, D. S., & Burrows, A. 2012, ApJ, 745, 174

[175] Storn, R., & Price, K. 1997, Journal of Global Optimization, 11, 341

[176] Su, K. Y. L., Rieke, G. H., Stapelfeldt, K. R., et al. 2009, ApJ, 705, 314

[177] Sudol, J. J., & Haghighipour, N. 2012, ApJ, 755, 38

[178] Suzuki, R., Kudo, T., Hashimoto, J., et al. 2010, in Proc. SPIE, Vol. 7735, 30

[179] Swift, J. J., Bottom, M., Johnson, J. A., et al. 2015, Journal of Astronomical Telescopes, Instruments, and Systems, 1, 027002

[180] Tamura, M. 2009, in American Institute of Physics Conference Series, ed. T. Usuda, M. Tamura, & M. Ishii, Vol. 1158, 11

[181] Tamura, M., Suto, H., Nishikawa, J., et al. 2012, in Society of Photo-Optical Instrumentation Engineers (SPIE) Conference Series, Vol. 8446, 1

[182] Tegmark, M., Strauss, M. A., Blanton, M. R., et al. 2004, Phys. Rev. D, 69, 103501

[183] Thalmann, C., Janson, M., Buenzli, E., et al. 2011, ApJ, 743, L6

[184] Thiele, T. 1883, Astronomische Nachrichten, 104, 225

[185] Tokovinin, A. 1992, in Astronomical Society of the Pacific Conference Series, Vol. 32, IAU Colloq. 135: Complementary Approaches to Double and Multiple Star Research, ed. H. A. McAlister & W. I. Hartkopf, 573

[186] Tokovinin, A. 2014, AJ, 147, 86

[187] Tokovinin, A. A. 1993, Astronomy Letters, 19, 73

[188] Van den Bos, W. H. 1932, Circular of the Union Observatory Johannesburg, 86, 261

[189] van Leeuwen, F. 2007a, A&A, 474, 653

[190] van Leeuwen, F. 2007b, A&A, 474, 653

[191] Veras, D., Crepp, J. R., & Ford, E. B. 2009, ApJ, 696, 1600

[192] Vorobyov, E. I. 2013, A&A, 552, A129

[193] Wilson, P. A., Hébrard, G., Santos, N. C., et al. 2016, ArXiv e-prints, 1602.02749

[194] Wolszczan, A. 1994, Science, 264, 538

[195] Wolszczan, A., & Frail, D. A. 1992, Nature, 355, 145

[196] Wright, D. J., Chené, A.-N., De Cat, P., et al. 2011, ApJ, 728, L20

[197] Wright, J., & Howard, A. 2012, RVLIN: Fitting Keplerian curves to radial velocity data, Astrophysics Source Code Library

[198] Wright, J. T., & Howard, A. W. 2009, ApJS, 182, 205

[199] Zuckerman, B., Rhee, J. H., Song, I., & Bessell, M. S. 2011, ApJ, 732, 61

[200] Zurlo, A., Vigan, A., Galicher, R., et al. 2016, A&A, 587, A57